Journal of Sound and Vibration 582 (2024) 118423

Contents lists available at ScienceDirect

Journal of Sound and Vibration

journal homepage: www.elsevier.com/locate/jsvi

# Aerodynamic noise analysis of tilting rotor in edgewise flow conditions

Nur Syafiqah Jamaluddin [a,b,*], Alper Celik [a,c], Kabilan Baskaran [a,d], Djamel Rezgui [a], Mahdi Azarpeyvand [a]

[a] School of Civil, Aerospace and Design Engineering, University of Bristol, Bristol, BS8 1TR, UK
[b] Jaguar Land Rover, Banbury Road, Gaydon, Warwick, CV35 0RR, UK
[c] Department of Aerospace Engineering, Swansea University, Swansea, SA1 8EN, UK
[d] Department of Mechanical Engineering, Indian Institute of Technology (Indian School of Mines), Dhanbad, 826004, IN

ARTICLE INFO

*Keywords:*
Rotor noise
Aeroacoustics
Tilt rotor
Wind tunnel experiment
Urban air mobility

ABSTRACT

This paper presents a comprehensive experimental analysis of the noise characteristics of an isolated tilt-rotor system under edgewise flight conditions. The investigation explores the effect of rotor tilt on noise and aerodynamics using flow velocity, thrust, and far-field noise measurements. Flow field results show that as the tilting angles vary, there is a change in speed over the rotor blade surface, which influences vortex formation and wake attributes. The far-field noise spectra revealed a significant decrease in sound pressure level with increasing tilt angle, predominantly evident in both the high-amplitude tonal peaks and the broadband signal within the low-to-mid frequency range. The directivity patterns of the overall sound pressure level also demonstrated a reduction in magnitude with the tilting of the rotor. This reduction was observed consistently across all top-plane observation points, with a monopole directivity trend. Meanwhile, in the side plane array, the decrease was primarily evident above the plane of rotation with a dipole directivity pattern. The radiation direction at which the minimum sound pressure level occurs was identified near the rotation plane, irrespective of the tilt angle. Furthermore, the time-dependent noise analyses revealed dominant and persistent signal characteristics at the blade passing frequency, whereas the mid-frequency range exhibited more intermittent behaviour, and the high-frequency range indicated transient characteristics.

## 1. Introduction

The noise produced by rotating blades has long been a subject of global scientific interest. This field has become particularly significant in recent years due to the emergence and rapid expansion of the Urban Air Mobility (UAM) industry. As this sector continues to evolve, the demand for extensive aeroacoustic investigations intensifies to facilitate the design of quieter aircraft for UAM. This pursuit is driven by safety considerations and the pressing environmental challenge of noise pollution. The sound emissions from electrically driven propellers of this emerging mode of transport carry broad implications, affecting both the environment and public acceptance [1,2]. Therefore, the challenge lies in achieving a twofold objective: first, minimising decibel levels to ensure regulatory compliance, and second, effectively managing the noise footprint in densely populated metropolitan areas and around Vertiports [3–5].

* Corresponding author.
*E-mail addresses:* njamalud@jaguarlandrover.com (N.S. Jamaluddin), alper.celik@swansea.ac.uk (A. Celik), kabilan@iitism.ac.in (K. Baskaran), djamel.rezgui@bristol.ac.uk (D. Rezgui), m.azarpeyvand@bristol.ac.uk (M. Azarpeyvand).

https://doi.org/10.1016/j.jsv.2024.118423
Received 8 November 2023; Received in revised form 20 March 2024; Accepted 31 March 2024
Available online 3 April 2024

The tilt-rotor concept, an innovative design that enables aircraft propellers or rotors to pivot from a vertical to a horizontal orientation, was first developed in the 1950s. The Vertol VZ-2 was a pioneering example of this technology, successfully demonstrating multiple transitions between hovering and forward flight [6]. Today, this innovative design is a core component of many Vertical Takeoff and Landing (VTOL) aircraft, particularly within the UAM sector.[1] This mechanism allows UAM vehicles, such as air taxis and passenger drones, to take off and land vertically, similar to conventional helicopters, with rotors progressively tilting for forward flight, resembling a turboprop aeroplane. This unique combination of vertical lift and high-speed cruising ability allows efficient navigation within complex urban environments without the need for long runways [7].

From an aerodynamic perspective, the rotor blades of a tilt-rotor system encounter a highly complex flow field during the transition from vertical to horizontal flight, leading to intricate aerodynamic interactions that directly impact blade loading conditions [8,9]. The tilting of the rotor disc changes the angle at which the rotor blades interact with the incoming airflow. Ho and Yeo conducted a comprehensive study on the aerodynamic loading of rotor blades of several existing helicopters in forward flight [10]. The key observations from this study involve the flow structure and specific aerodynamic challenges that a typical helicopter rotor faces in forward flight. Using an isolated system, the study represented rotor blades as lifting lines divided into several 'aerosegments'. Each segment produces a complex vortex-rich flow at the near-wake region, which comprises a combination of trailing and shedding vortices. The latter are shed at every blade rotation considering the change in azimuthal position. Beyond this point, a less complex far-wake model was considered, comprising a discrete tip vortex and a large-core vortex, representing the inboard wake sheet trailing across the entire blade span.

Like other rotary-wing systems, tilt-rotors also exhibit a similarly complex sound generation mechanism. This complexity is further increased due to the transition process intrinsic to their operation, making the understanding and managing of noise a significant challenge. The noise produced by isolated tilt-rotors consists of tonal and broadband elements. The tonal part of this noise spectrum is generated at the blade passing frequency and its harmonics. The tonal noise contribution, which is deterministic in nature, recurs with every rotation of the rotor blade. Tonal noise primarily depends on the rotor's operational conditions, influenced by its tip speed and the flow condition it encounters [11,12]. Predominantly, two main mechanisms are responsible for generating this tonal component: the loading noise and thickness noise. The former results from the aerodynamic forces exerted on the rotating blades relative to the surrounding air, while the latter derives from fluid displacement by the blade surfaces [13]. In this study, the role of thickness noise is negligible due to the low tip Mach number considered, which is less than 0.7 [14]. Meanwhile, the variation in the unsteady loading noise caused by blade-vortex interactions (BVI) is more dominant, particularly in the case of rotors in edgewise flight. BVI occur when the tip vortex or unsteady wake of a preceding blade impacts the successive blade, resulting in high amplitude tonal noise repeated precisely at the harmonics of the BPF at each blade revolution [15]. During the edgewise flight, the tip vortices of the blade can be ingested into the rotor and cause a rapid and local change in the angle of attack and a sudden change in blade load [13]. In addition to these tonal noise sources, rotor noise also comprises broadband noise, which is stochastic in nature, is mainly generated by turbulent flow across the tilt-rotor, significantly contributed by both turbulent boundary-layer trailing-edge noise and turbulence ingestion noise at the leading edge [16] and the boundary-layer interactions of the rotor blade with its wake [17].

While many preceding studies have delved into the acoustics study of a small-scaled rotor in edgewise configuration, such as found in [18–22], most of these studies focused on a single and fixed position without much attention to the effects of skewed inflow caused by tilting the rotor disc. Yang et al. conducted an experimental study on the influence of the shaft angle on the aerodynamic and aeroacoustic performance of a multicopter rotor during forward flight conditions, tested at a rotational speed of 6000 rpm [23]. Their work demonstrated the impact of the shaft angle on multicopter performance metrics, including thrust, power, moments, and Sound Pressure Level (SPL). The study observed that increasing shaft angle, with a constant rotation speed, decreases these performance indicators. However, the analysis and interpretation of why lower shaft angles corresponded to higher SPLs were limited, and the study did not include a flow visualisation. A more detailed understanding of this relationship would therefore provide better insight into the mechanisms by which the shaft angle influences noise generation and propagation. The rotor size and the range of shaft angles tested were also restricted in Yang et al. study. Their tested rotor was only 8 inches in diameter, nearly 43% smaller than the rotor tested in the present study. Despite these limitations, their study provides an invaluable foundation for further research.

Therefore, the present study aims to provide a detailed analysis of the effects of shaft angle on rotor noise characteristics. The investigation involves a comprehensive experimental analysis of noise generated by a small-scale tilt-rotor under hovering and edgewise flight conditions. The present study investigates aerodynamics' impact on the acoustic signature and visualises the flow field at each position. The paper is organised as follows. Section 2 introduces the experimental setup, detailing the tilt-rotor rig and instrumentation. Section 3 provides a detailed discussion of the results in five sub-sections. Section 3.1 presents the loading and the flow field characteristics of the rotor. The characterisations of noise spectra are discussed in Section 3.2, followed by Section 3.3, which focuses on the directivity trend of the overall sound pressure level. Section 3.4 specifically highlights the contribution from the multiple harmonic tones, while Section 3.5 presents findings on the time-dependent nature of the radiated noise. Finally, the paper is concluded with Section 4, where we summarise the findings and present some remarks for future studies.

[1] https://evtol.news/aircraft.

## 2. Experimental methodology

### 2.1. Measurement setup

Investigations on the tilting effects of an isolated rotor were performed at The University of Bristol's aeroacoustics facility, which comprises a closed-circuit open-jet wind tunnel with a large anechoic chamber. The chamber dimensions were 7.9 m × 5.0 m × 4.6 m (L × W × H), with a cut-off frequency of 160 Hz. For the current studies, a nozzle measuring 0.5 m in width and 0.775 m in height was utilised, providing a reliable speed range between 5 to 40 m/s and a nominal turbulence intensity level of 0.2%. A detailed description of the facility can be found in Mayer et al. [24].

An off-the-shelf two-bladed APC propeller with 0.3048 m diameter and 0.1016 m geometrical pitch was employed in the study, which corresponds to a pitch-to-diameter ratio of 0.3. The rotor was tested at various tilting angles, from 0° to 30°. These angles were measured from the upright position of the rotational axis (zero tilt) to the position when the rotor disc was tilted. The rotor blade was driven by a 40 A speed-controlled brushless motor powered by a DC bench power supply, regulated up to a maximum of 25 V. The motor speed was modulated by varying the throttle settings of the Electronic Speed Control (ESC), and the resulting electrical current was measured at the power supply. The rotor blade rotation speed was determined by measuring the electrical pulse signals from one of the three wires of the brushless DC motor. A reading of the rotation speed was also obtained using a DT-2234C+ reflective optical sensor, providing a one-per-revolution signal of the motor casing. The aerodynamic loading data were collected using an ATI Mini40E 6-axis load cell, calibrated by the manufacturer for a measurement uncertainty at the 95% confidence level. A National Instruments PXIe-1082 data acquisition system simultaneously captured loading and far-field noise data for 16 s at a sampling rate of $2^{16}$ Hz.

The rotor was positioned at the centre of the open jet nozzle, approximately 0.6 m from the nozzle exit, as illustrated in the schematics drawing of the experimental setup in Fig. 1. Acoustic measurements were recorded using 37 GRAS Sound and Vibration model 40PL $\frac{1}{4}$ inch-diameter microphones, with an upper limit of 142 dB and a frequency range of 10 Hz to 20 kHz. The microphones were installed on a far-field overhead and side plane arc, capturing noise measurements within top plane observation points of $\theta = 40°$ to 150°, and the side array angles between $\phi = +75°$ and $-55°$, as illustrated in 1. The microphone arrays were located at distances from the rotor's plane of rotation proportionate to the rotor diameter, $D$. The top array was placed at a distance of $5D$, while the side array was positioned at a distance of $3D$. A distance correction factor was applied to the data to compare both microphone arrays (top and side), assuming spherical wave propagation in a free field. Background noise data was also acquired to quantify other undesirable noise sources, such as background flow noise, reflective surfaces and unloaded electrical motor noise [25].

### 2.2. Analysis method

The rotor aerodynamic performance was evaluated using the thrust data measured at the blade hub along the rotational axis. The measurements were taken for 16 s. The thrust values are then normalised in the form of non-dimensional thrust coefficients, $C_T$, defined as,

$$C_T = \frac{T}{\rho(\Omega R)^2 A} \quad , \tag{1}$$

where $\rho$ is the air density, $A$ is the rotor disc area, and $T$ is the time-averaged aerodynamic thrust force exerted along the rotor's rotational axis and normal to the rotor disc. When transitioning from a vertical lift position (i.e. $\alpha = 0°$) to a forward tilt position (i.e. $\alpha > 0°$), the rotor blade encounters changes in the aerodynamic conditions. These changes influence the periodically varying aerodynamic load produced by the rotor blade.

Furthermore, particle Image Velocimetry (PIV) was also employed to visualise the influence of the tilting angles on the flow field surrounding the blade. The illumination was achieved with a 200 mJ Nd:YAG dual-cavity laser at a repetition rate of 15 Hz. The images were recorded by a 4 MP FlowSense CCD (Charge-Coupled Devices) camera with a 2048 × 2048 pixels resolution. Measurements were taken on the x-z plane near the rotor blade's hub for a field view of 310 mm × 310 mm, which corresponded to a domain of $2R \times 2R$ in the streamwise and vertical directions. The laser sheet was located at $z = 0.2R$, as shown schematically in Fig. 2(b). A total number of 1200 image pairs were captured to calculate the time-averaged velocity field for each case. The instantaneous velocity vector fields were calculated via Dantec DynamicStudio software with an interrogation window of 16 pixels x 16 pixels, which yields an effective grid size of 1.5% of the blade's radius (0.14 mm/px). The DynamicStudio software was also used to conduct the uncertainty analysis of the images following the uncertainty quantification methodology detailed in [26,27], ensuring precise peak detection and displacement estimation. The assessment method takes into account the sub-pixel displacement of seeding particles within the interrogation windows of each image pair, as well as the cross-correlation analysis used to determine particle displacement and instantaneous airflow velocity. The uncertainty in the measurements was found to be less than 1%.

Fig. 2(a) illustrates the projection of various loading and velocity components acting on a rotor, positioned at a tilting angle of $\alpha$ under an edgewise inflow condition. The freestream velocity $U_\infty$ is approaching the rotor from right to left. The in-plane projection of this velocity onto the rotor disc can be mathematically defined as $U_i = U_\infty \cos\alpha$, while the out-of-plane is $U_o = U_\infty \sin\alpha$. The aerodynamic forces exerted on the rotor, such as the thrust and torque, are represented in the figure by $T$ and $Q$, respectively.

The far-field noise results are presented in terms of the frequency-dependent energy content of the pressure fluctuations. The energy content is expressed in terms of the sound pressure level (SPL) in dB and is calculated as,

$$\mathrm{SPL} = 10\log_{10}\left(\frac{\phi_{pp}}{p_{ref}^2}\right) \tag{2}$$

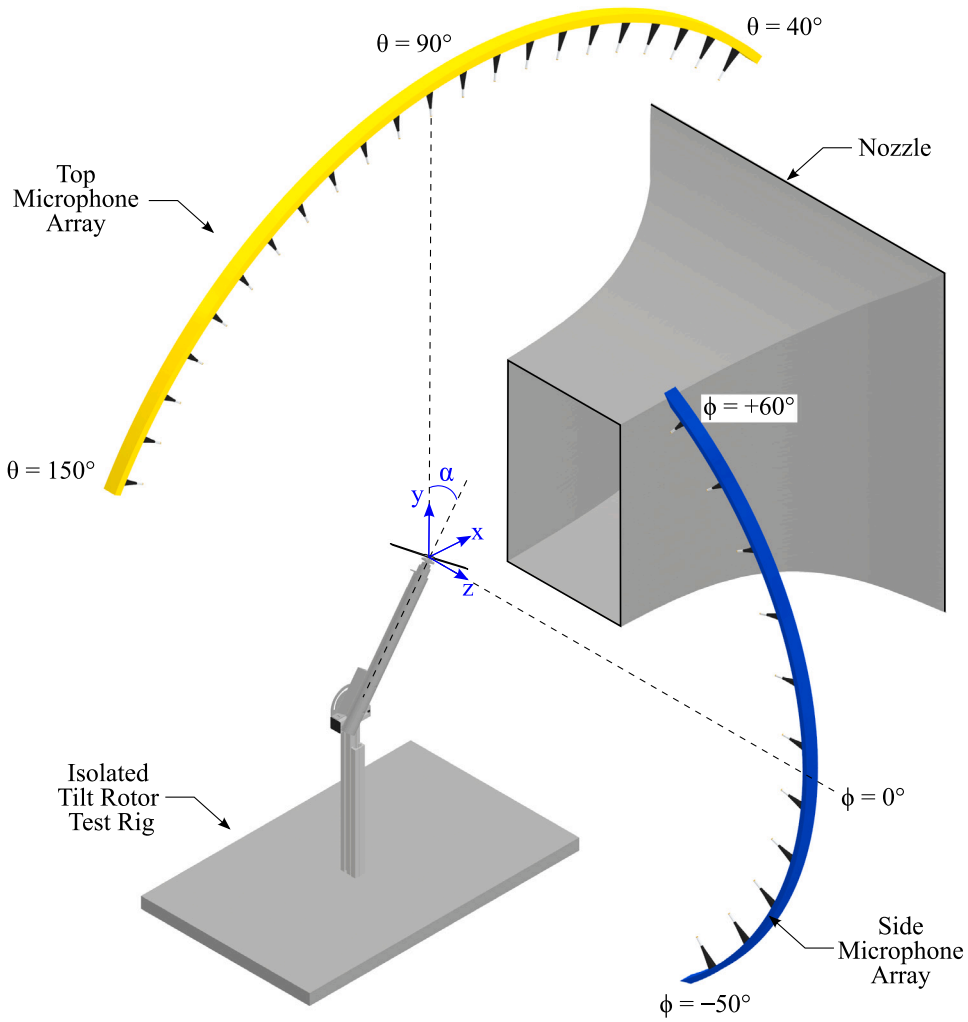


**Fig. 1.** Schematics of the wind tunnel setup with the test rig, microphone arrays in the top and side planes. The definition of the tilting angle, $\alpha$, and the global coordinate system are also illustrated.

where $\phi_{pp}$ is the power spectral density of the measured far-field pressure fluctuations, and $p_{ref} = 20$ μPa is the reference sound pressure. The power spectral density of the pressure fluctuations ($\phi_{pp}$) was estimated by using Welch's method [28], where the data from the transducers are segmented for 32 equal lengths with 50% overlap and windowed by the Hamming function, resulting to a frequency resolution of $\Delta f = 2$ Hz. The data obtained yields an absolute uncertainty of ±0.05 dB with a 95% of confidence level.

The overall sound pressure levels (OASPL) derived from the top and side microphone arrays are analysed to provide characteristics of the far-field directivity of the radiated noise for rotors at various tilting angles. The OASPL of the far-field noise was calculated by integrating the acoustic energy spectrum with respect to frequency over the frequency range 100 Hz $< f <$ 20,000 Hz as,

$$\mathrm{OASPL} = 10 \cdot \log_{10}\left[\frac{\int \mathrm{PSD}(f)\, df}{p_{ref}^2}\right], \tag{3}$$

where PSD($f$) is the power spectral density of the sound pressure, and $p_{ref}$ is the conventional reference pressure of 20 μPa.

The wavelet transform method is also employed to analyse the acoustic pressure time signal from the rotor, denoted $p(t)$. The method involves projecting the input signal onto a compact set of support functions, referred to as wavelets, that are localised in both time and frequency domains. The wavelet transform of the signal ($w(s,\tau)$) is the inner product between $p(t)$ and the wavelet family $\psi(t)$, that is,

$$w(s,\tau) = s^{-1/2}\int_{-\infty}^{\infty} p(t)\psi^*\left(\frac{t-\tau}{s}\right) dt, \tag{4}$$

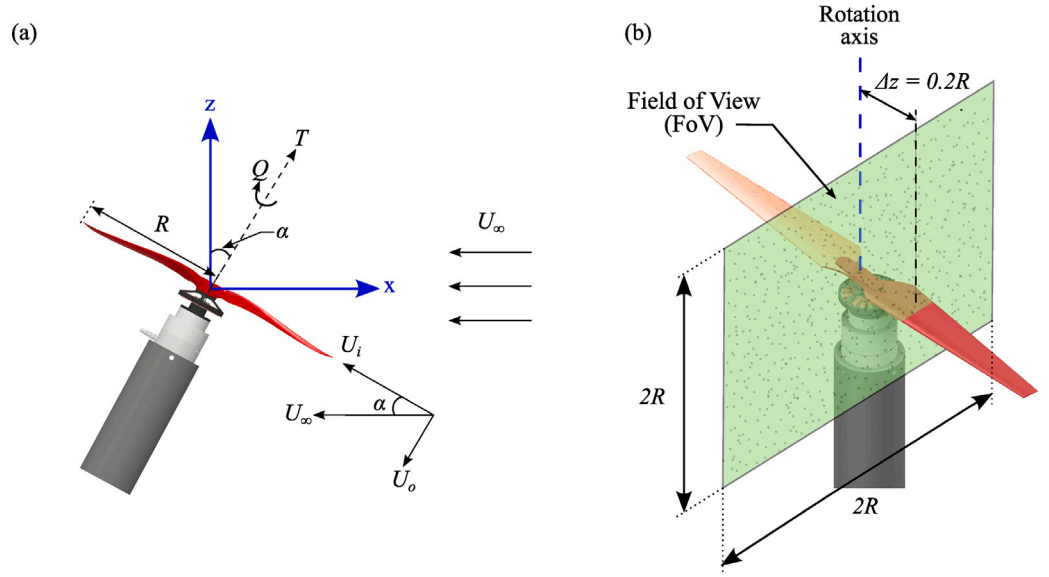


**Fig. 2.** Schematics representation of (a) a rotor blade in tilted edgewise flight condition, illustrating key aerodynamic forces and velocity components during edgewise inflow conditions adopted from [23], and (b) the definition of field of view for PIV measurement. The definition of the tilting angle, $\alpha$, and the global coordinate system are also illustrated.

where $s \in \mathfrak{R}^+$ is the scale dilation parameter, and $\tau \in \mathfrak{R}$ is the translation parameter corresponding to the position of the wavelet in the physical space. The term $\psi^*\left(\frac{t-\tau}{s}\right)$ represents the complex conjugate of the mother wavelet $\psi(t)$, which was dilated and translated. A detailed explanation of the method is available in Refs. [29,30].

## 3. Results and discussion

This section details the experimental findings, starting with the presentation of the aerodynamic load data and its correlation with the velocity field obtained through PIV measurements. Subsequently, far-field acoustic results are analysed by comparing the spectral and directivity characteristics of the rotor noise at various tilt positions using the measurement from both the top and side plane arrays. Finally, the results of the time-frequency analyses of the acoustic data are presented to explore the intermittent and persistent characteristics of the radiated noise. The test was performed at a constant rotational speed of $\Omega = 5500$ rpm, corresponding to a blade passing frequency of approximately 183 Hz. This speed was selected to ensure compatibility with the cut-off frequency of the anechoic chamber, which is 160 Hz, and to closely align with the rotational speeds used in existing literature [23,31]. The mean freestream velocity, $U_\infty$, was varied between 0 to 20 m/s, corresponding to a range of advance ratio, $\mu$, between 0.09 to 0.34. The advance ratio was calculated considering the influence of the tilting angle ($\alpha$), inflow velocity, rotational speed ($\Omega$), and the radius of the blade ($R$), such that $\mu = U_\infty \cos\alpha / \Omega R$.

### 3.1. Loading performance and flow field characteristics

Fig. 3 presents the thrust coefficient of the rotor under varied tilting angles and inflow velocities. The results demonstrate a consistent decrease in the $C_T$ with an increase in tilting angle across all tested inflow velocities, as shown in Fig. 3(a). The decrease in the thrust coefficient with increasing tilt angles can be explained using the Blade Element Momentum Theory (BEMT), based on the assumption that the blade can be radially discretised into a series of small two-dimensional elements or sections along its length. Each blade element can be considered as a rotating lifting surface, where the local aerodynamic forces and moments are evaluated at each section then integrated along the blade span.

Fig. 4 presents an illustration of the flow velocity components and the aerodynamic forces acting on a blade section at any azimuth position, $\psi$. Here, the datum rotor blade's azimuth angle $\psi = 0°$ is located at the rear of the propeller disc. $\phi$, $\beta$, and $\alpha'$ denote the blade's elemental inflow angle, pitch angle and local angle of attack, respectively. It can be seen from Fig. 4 that the blade section is subjected to a flow velocity vector, $V_R$, which can be decomposed into a horizontal flow component, $V_t$, tangential to the plane of rotation and a vertical flow velocity component, $V_p$, perpendicular to plane of rotation. Considering the effect of the rotor tilt angle, $\alpha$, and the freestream velocity, $U_\infty$, these velocity components can be given as:

$$V_t = \Omega r + U_\infty \cos\alpha \sin\psi \tag{5}$$

$$V_p = U_\infty \sin\alpha + V_i, \tag{6}$$

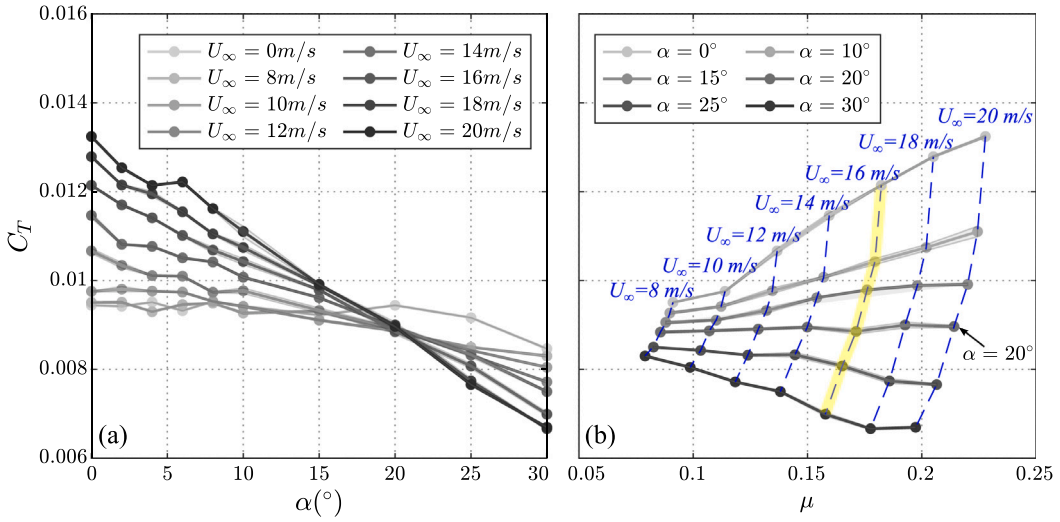


**Fig. 3.** Comparisons of thrust coefficients relative to the (a) tilting angles and (b) advance ratios at a constant rotation speed of 5500 rpm. The highlighted case in yellow corresponds to the operational conditions that were tested in the PIV analysis at $U_\infty = 16$ m/s. (For interpretation of the references to colour in this figure legend, the reader is referred to the web version of this article.)

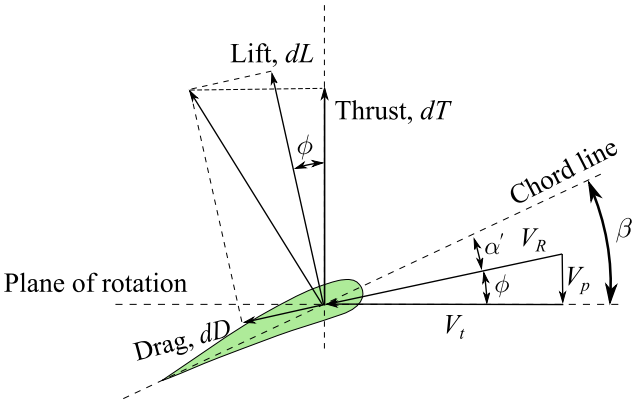


**Fig. 4.** The two-dimensional force and velocity components acting on a rotating propeller blade section.

where $\Omega$ is the rotational speed of the blade, $r$ is the radial distance of the element from the rotational axis, and $V_i$ is the induced velocity. Meanwhile, $dL$, $dD$, and $dT$ are the elemental aerodynamic lift, drag and thrust forces respectively, generated by the blade element.

From Eqs. (5) and (6), it can be shown that for a given freestream velocity, $U_\infty$, increasing the propeller tilt angle, $\alpha$, reduces the perpendicular flow component, $V_p$, while it reduces the tangential velocity component in the advancing side ($0^\circ < \psi < 180^\circ$) and increases it in the retreating side ($180^\circ < \psi < 360^\circ$). In all cases, it can be shown that these changes in the flow velocity components due to increasing the tilt angle, $\alpha$, will lead to an increase in the inflow angle, $\phi$, which will in-turn reduces the local elemental angle of attack, $\alpha'$ and hence the lift generated by the blade element, for non-stalled cases. Therefore, increasing the propeller tilt angle will decrease the thrust produced by the blade element and eventually by the whole propeller. The reduction in thrust will lead to a small decrease in induced velocity, $V_i$, but this change is not large enough to reverse the effects of increasing the propeller tilt, $\alpha$, on the inflow angle, $\phi$, and the local angle of attack, $\alpha'$. Example cases illustrating the changes in $V_t$, $V_p$, $\alpha'$ and $dL$ with variation of propeller tilt angle are provided in Fig. 5.

In addition to aerodynamic effects, rotor tilting also impacts the loading noise. The decrease in thrust coefficient at higher tilt angles correlates with reductions in tonal noise at the blade passing frequency ($m = 1$). This reduction in sound pressure level with increased tilting is shown in Figs. 8 and 9, and is explored in more detail in Section 3.2. The change in $C_T$ with respect to $\alpha$ also increases with inflow velocity, as shown by the increased magnitude of thrust coefficients for higher inflow velocity cases, specifically when the inflow velocity reaches approximately $U_\infty \geq 12$ m/s. This observation indicates that the thrust coefficient is more sensitive to changes in the tilting angle under higher inflow velocity. The results also reveal that at $\alpha = 20^\circ$, the thrust coefficients remain consistently comparable across different inflow speeds. Furthermore, at higher tilting angles of $\alpha > 20^\circ$, a decrease in $C_T$ was

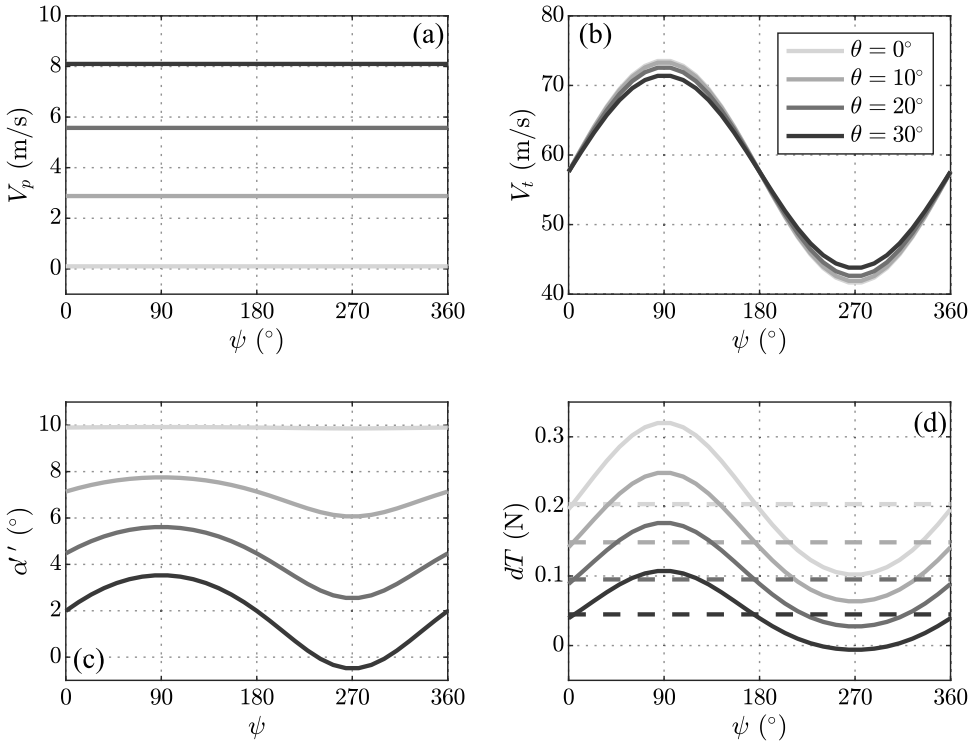


**Fig. 5.** Example aerodynamic quantities of a spinning blade element, over azimuth angle, $\psi$, for varying tilt angles at a constant inflow velocity of 16 m/s and rotational speed of 5500 rpm. Representative values were used for the blade element parameters and aerodynamic conditions. (a) Perpendicular velocity component $V_p$, (b) Tangential velocity component $V_t$, (c) Local angle of attack of the blade element, $\alpha'$, and (d) Elemental thrust $dT$, calculated using standard BEMT [32]. Dashed lines in (d) represent the mean $dT$ values in one revolution.

observed with increasing inflow velocity. The thrust coefficient ($C_T$) is also represented as a function of advance ratio ($\mu$), as shown in Fig. 3(b), over a range of inflow velocities between $U_\infty = 0$ to 20 m/s to explore the variations in $C_T$ at each tilting position. In the case of the vertical edgewise position, $\alpha = 0°$, the thrust coefficient increases from 0.0095 at 8 m/s to 0.0133 at 20 m/s. Meanwhile, at $\alpha = 20°$, $C_T$ remained nearly constant, with an average of approximately 0.0089 across all tested inflow velocities. Conversely, at $\alpha = 30°$, the thrust coefficient decreases from 0.0083 at 8 m/s to 0.0067 at 20 m/s.

To elucidate the state of the flow with varying tilt angles, two analyses were performed on the PIV data. First, the velocity flow field was examined to visualise the flow ingestion, flow acceleration and downwash flow regions at different tilting angles. Subsequently, the mean turbulent kinetic energy ($TKE$) levels were analysed to quantify the energy content within the flow field and, more specifically, within the regions where turbulence ingestion has occurred. The PIV measurements were performed under varying tilting angles at a freestream velocity of 16 m/s and a constant blade rotation speed of 5500 rpm, as indicated in Fig. 3. The mean velocity and TKE results will be again later used in Section 3.2 to explain any noise increase due to turbulence ingestion. The tilting effects were analysed within a tip-to-tip domain from $x = -1R$ to $x = +1R$, where $R$ represents the radius of the blade. The measurements were taken on the $x$–$y$ plane adjacent to the hub of the rotor with an offset along the $z$-axis by approximately $0.2R$. This location sat on the advancing side of the rotor disc, which experienced higher velocity components in edgewise flight conditions compared with the retreating side of the rotor.

In the vertical hovering position ($\alpha = 0°$), as shown in Fig. 6(a), the flow is observed to be drawn from the upstream half of the blade to the downstream half, generating a strong wake structure behind the rotor. This interaction results in localised acceleration zones, evidenced by the increased velocity, particularly within the domain both upstream of the rotor and above the rotation plane (i.e. $y/R > 0$ and $x/R > 0$) as well as within the wake of the blade below the rotation plane (i.e. $y/R < 0$ and $x/R < 0$). As the tilting angles increase, two main flow behaviours emerge. Firstly, the flow region above the upstream half of the rotor appeared to be less disturbed and reduced in acceleration. Secondly, at the wake of the rotor, the region of accelerated flow expands, especially between $-1 \leq x/R \leq +0.5$, and becomes more pronounced at higher tilting angles.

The PIV data were further analysed to evaluate the mean $TKE$, allowing for clearer visualisation of specific points within the flow field. The mean turbulent kinetic energy was calculated as, $TKE = 0.5(\overline{u}^2 + \overline{v}^2)$, where $\overline{u}$ and $\overline{v}$ were the root-mean-square values of the vertical and streamwise velocity components, respectively. Fig. 7 presents line plot representations of TKE values at specific streamwise locations on the rotor disc, under the same operating conditions. The results are presented at ten streamwise locations spanning from the blade's downstream tip ($x = -1.0R$) to the upstream tip ($x = +1.0R$) at increments of $0.2R$. To enhance clarity, the plane of rotation for the rotor during the non-tilting condition (i.e., $\alpha = 0°$), located at a vertical position of $y/R = 0$, is highlighted

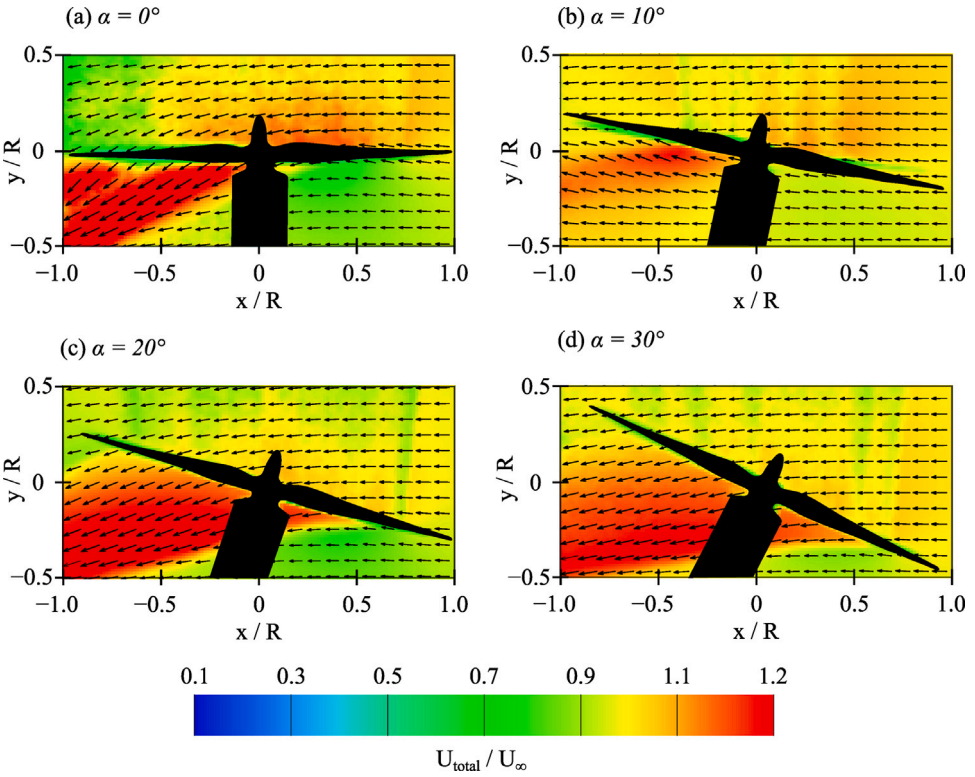


**Fig. 6.** Time-averaged total velocity contour normalised against the freestream velocity ($U_{total}/U_\infty$) for (a) $\alpha = 0°$, (b) $\alpha = 10°$, (c) $\alpha = 20°$, and (d) $\alpha = 30°$. These contours were obtained at a constant rotational speed of 5500 rpm and an inflow velocity of 16 m/s.

in the figure. At the tip region of the upstream half of the rotor (i.e. $x = +1.0R$), as shown in Fig. 7(e), $TKE$ levels are minimal for all tilt angle cases, indicating undisturbed and low turbulent kinetic energy in the flow. Moving towards the hub at $x = +0.2R$, as shown in Fig. 7(a), high levels of $TKE$ can be observed along the plane of rotation at $y/R = 0$, especially for $\alpha = 0°$. Within the downstream region, between $x/R = -0.2$ and $x/R = -1R$, as shown in Fig. 7(f)–(j), stronger $TKE$ levels can observed above the rotation plane. A large discrepancy between the vertical edgewise case ($\alpha = 0°$) and forward tilting cases ($\alpha > 0°$) is evident at the tip region of the downstream half of the blade, as seen in Fig. 7(f). These elevated levels of $TKE$ at $\alpha = 0°$ are representative of significant turbulence in the flow, which can be indicative of flow separation and increased aerodynamic losses. Such conditions can lead to higher induced drag, which contributes to the higher thrust coefficient observed at this angle, as shown in Fig. 3(b).

### 3.2. Far field noise spectra

Figs. 8 and 9 present the far-field noise spectra for an observer at $\theta = 90°$ (i.e., top array), and $\phi = 0°$ (i.e., side array), for the rotor at different tilting angles of $\alpha = 0°$, 10°, 20°, and 30°, and for different inflow conditions, namely $U_\infty = 0$, 12, 16 and 20 m/s. As before, the tests were performed using a two-bladed rotor ($b = 2$), at a constant rotation speed of $\Omega = 5500$ rpm, resulting in a blade-passage frequency of 183.33 Hz. In both Figs. 8 and 9, discrete tonal peaks occurring at the BPF and its harmonics dominate the frequency spectrum of up to 2000 Hz, irrespective of the rotor tilting angle. The non-dimensional number of the blade passing frequency, $m$, is defined as $m = f/\text{BPF}$, where $f$ is the frequency. In the figure $m = 1$ peak corresponds to the fundamental blade passing frequency, and the $m = 2$, and $m = 3$ peaks are the first and second harmonics of the BPF. As can be seen in Figs. 8 and 9, the results show that the SPL magnitude at the BPF decreases with the tilt angle, consistent with the observation of thrust coefficient in Fig. 3. The observed reduction in BPF amplitude with respect to the tilt angle can be attributed to the decrease in the thrust coefficient, i.e. steady loading acting on the blades as previously discussed in Section 3.1. As described in Section 3.1, the increase in the tilt angle of the rotor leads to a reduction in the mean thrust acting on the rotor in the flow regime. This leads to a consistent reduction of the noise at the blade passing frequency at all inflow velocity cases considered here. These decreases are particularly noticeable within the BPF and the first two harmonics (i.e. $m = 1$ to 3) in the frequency range 183 Hz $\leq f \leq$ 732 Hz, by approximately 2 to 10 dB. Nonetheless, the general trend remains consistent at higher frequencies, dominated by the blade's broadband self-noise.

At the hover condition, i.e., $U_\infty = 0$ m/s, as shown in Figs. 8(a) and 9(a), the SPL spectra are characterised by a high number of multiple harmonics peaks over a wide range of frequencies. Additionally, high amplitude sub-harmonic tonal components are also

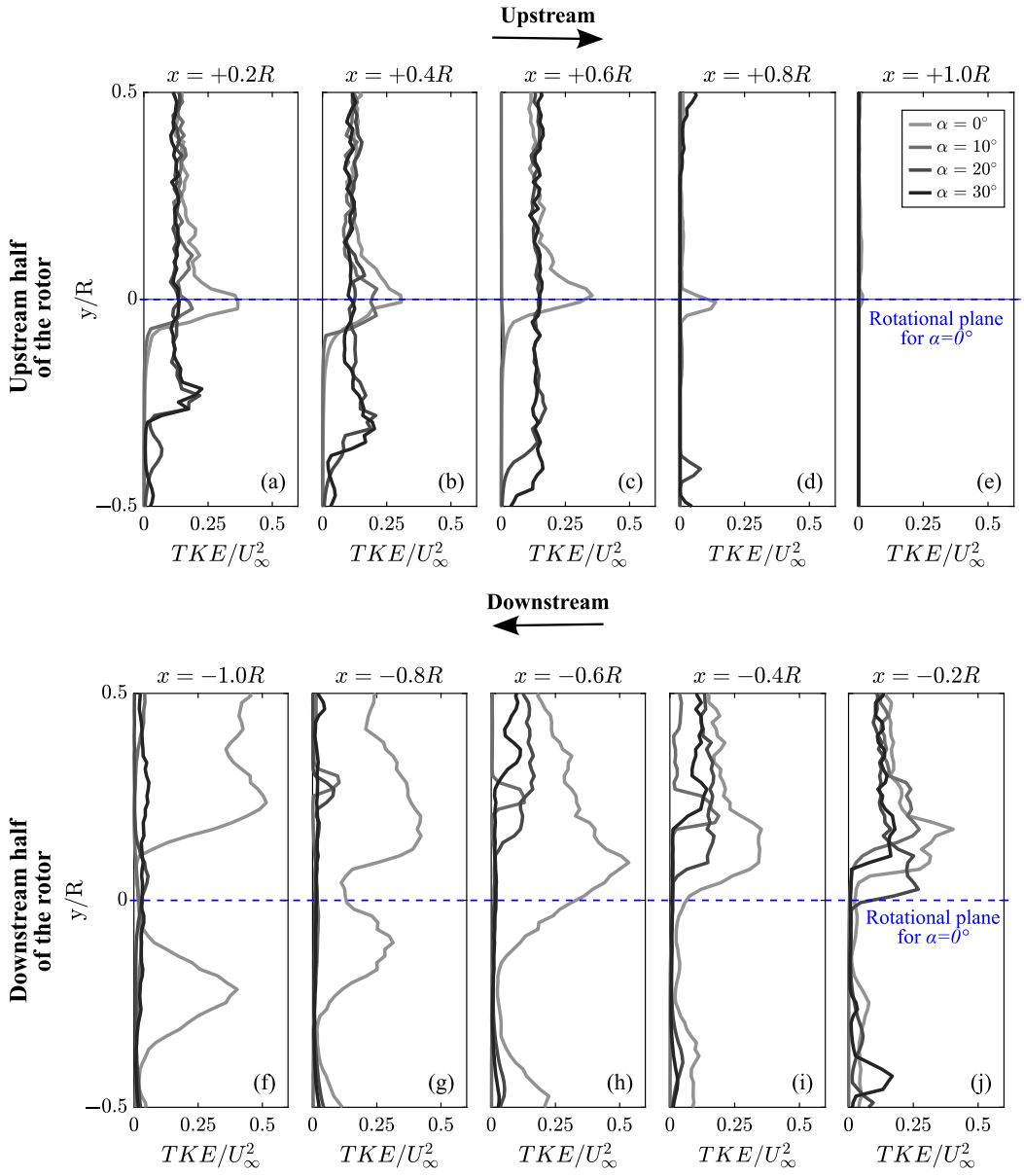


**Fig. 7.** The comparison of turbulent kinetic energy along the blade disc area, measured along the $x$–$y$ plane at $z = +0.2R$ for operation at constant 5500 rpm and 16 m/s inflow velocity. The results are presented for the upstream half of the rotor at streamwise positions of (a) $x = +0.2R$, (b) $x = +0.4R$, (c) $x = +0.6R$, (d) $x = +0.8R$, and (e) $x = +1.0R$, as well as at the downstream half of the rotor at (f) $x = -1.0R$, (g) $x = -0.8R$, (h) $x = -0.6R$, (i) $x = -0.4R$, and (j) $x = -0.2R$.

observed at $m = 1.5, 2.5, \ldots$, both from the top and side observation arrays, often regarded as the rotor shaft noise. As can be seen from Fig. 8(a), the $m = 1.5$ noise can be higher than the fundamental blade passing frequency noise in static conditions. As shown, the magnitude of the $m = 1.5$ noise can increase with the tilt angle, due to the aerodynamic loading and moment imbalance caused by the electric motor during this phase of operation. As can be seen in Figs. 8(b)–(d) and 9(b)–(d), increasing inflow velocities leads to a reduced number of these peaks, especially within the mid-to-high frequency ranges from $f = 2000$ Hz. The effect of tilting on the far-field spectra can be clearly observed in the non-zero inflow velocity cases, where the results for $\alpha = 30°$ case, for example, show the lowest magnitude of SPL within the frequency range between 183 Hz to 5000 Hz. Meanwhile, the highest SPL magnitudes are that of $\alpha = 0°$, which also corresponds to the rotor position where the aerodynamic load is the highest. The decrease in SPL, over the mid-frequency range (i.e. 1000 Hz to 5000 Hz), with tilting becomes more pronounced for rotor operating in higher inflow velocities, as evident in Figs. 8(d) and 9(d). As observed earlier in Fig. 3(b), the aerodynamic loading acting on the rotor also has its largest variation with $\alpha$ at high inflow velocity, consistent with the observation here for the radiated noise.

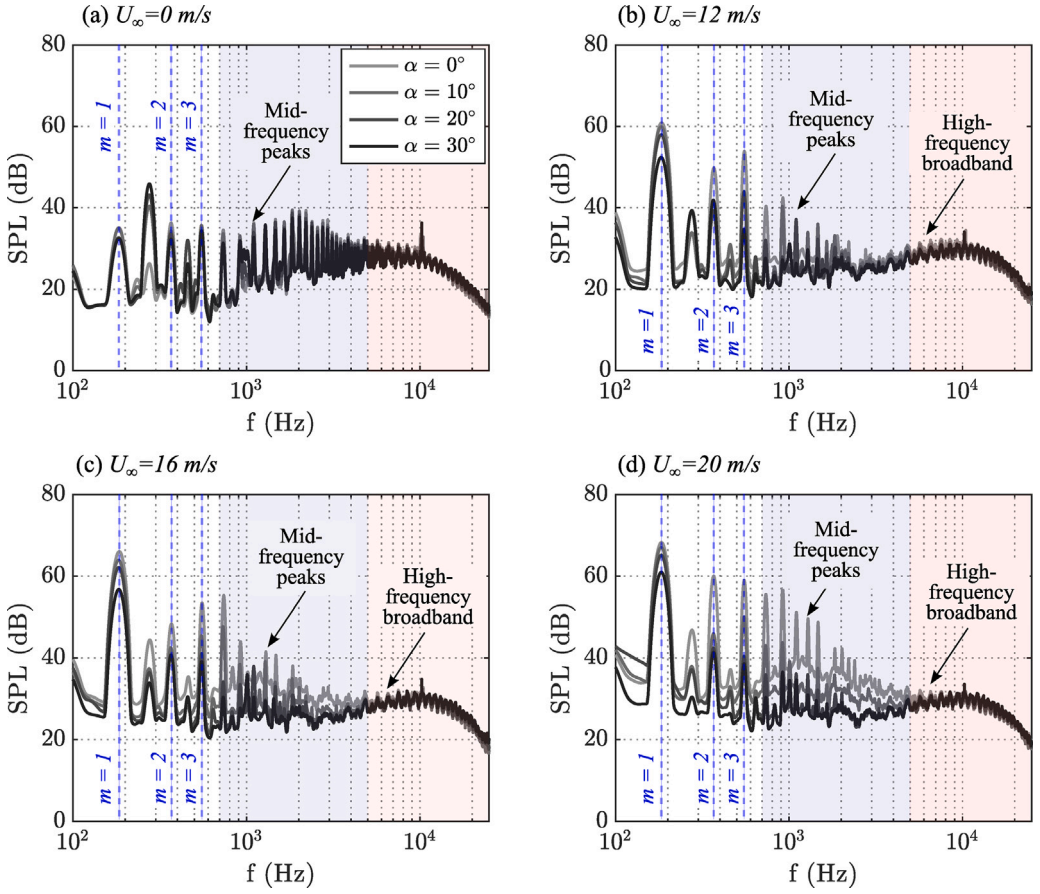


**Fig. 8.** Comparison of the far-field noise spectra at $\theta = 90°$ on the top array for (a) $U_\infty = 0$ m/s, (b) $U_\infty = 12$ m/s, (c) $U_\infty = 16$ m/s, and (d) $U_\infty = 20$ m/s.

At lower tilting angles and higher inflow velocities, the broadband noise levels in the mid-range frequencies are noticeably higher and more mid-frequency tonal peaks are present in the noise spectra, as seen in Figs. 8 and 9. The observed increase in broadband noise levels may be attributed to the increased blade self-noise across broad mid-range frequencies. Section 3.1 shows that at a hover position ($\theta = 0°$), the increase of flow velocity relative to the freestream velocity ($U_{total}/U_\infty$) occurs over the entire rotor disc surrounding the blade, as shown in Fig. 6(a). However, at higher tilting positions, the flow velocity increases predominantly in the wake of the blade as can be seen in Fig. 6(b), (c) and (d). These results suggest a complex flow pattern including turbulence and flow separation at $\alpha = 0°$, which become more significant at higher inflow velocities due to the level of separation and interaction with the blade. On the other hand, the presence of the mid-frequency tonal peaks is likely linked to the re-ingestion of tip vortices interacting with the blades. The frequencies of these tonal peaks correspond to the higher-order integer multiples of the BPF, influenced by the rotor's periodic rotational dynamics. This blade-tip vortex interaction is significantly influenced by the energy content of the flow interacting with the rear half of the rotor disc, as evidenced by the increased turbulence kinetic energy of the flow near blade tip at a non-tilting position, as shown in Fig. 7(f). Meanwhile, the high-frequency noise remained relatively comparable across various rotor tilting angles and inflow velocities, which suggests that the primary source of high-frequency broadband noise, i.e. the blade self-noise, is less affected by the tilt angle and that the state of unsteady loading acting on the blade has not changed greatly over this tilting range.

### 3.3. Directivity of overall sound pressure level

Fig. 10 presents the OASPL directivity of the rotor noise for ten tilting positions, ranging from $\alpha = 0°$ to $\alpha = 30°$, at different inflow velocities. The data are collected using the top microphone array, see Fig. 1, over $40° \leq \theta \leq 140°$. Fig. 10(a) shows the results for the static thrust condition of $U_\infty = 0$ m/s, and Fig. 10(b)–(d) present the results at inflow velocity of $U_\infty = 12$, 16 and 20 m/s, respectively. Under the static thrust condition, i.e. $U_\infty = 0$ m/s, as shown in Fig. 10(a), the rotor's tilting angle was found to have minimal influence on the OASPL over the observation locations of $40° \leq \theta \leq 90°$. However, there is a noticeable difference in the OASPL by about 3 to 4 dB between the case of $\alpha = 0°$ and 30° over $90° \leq \theta \leq 140°$ observation positions.

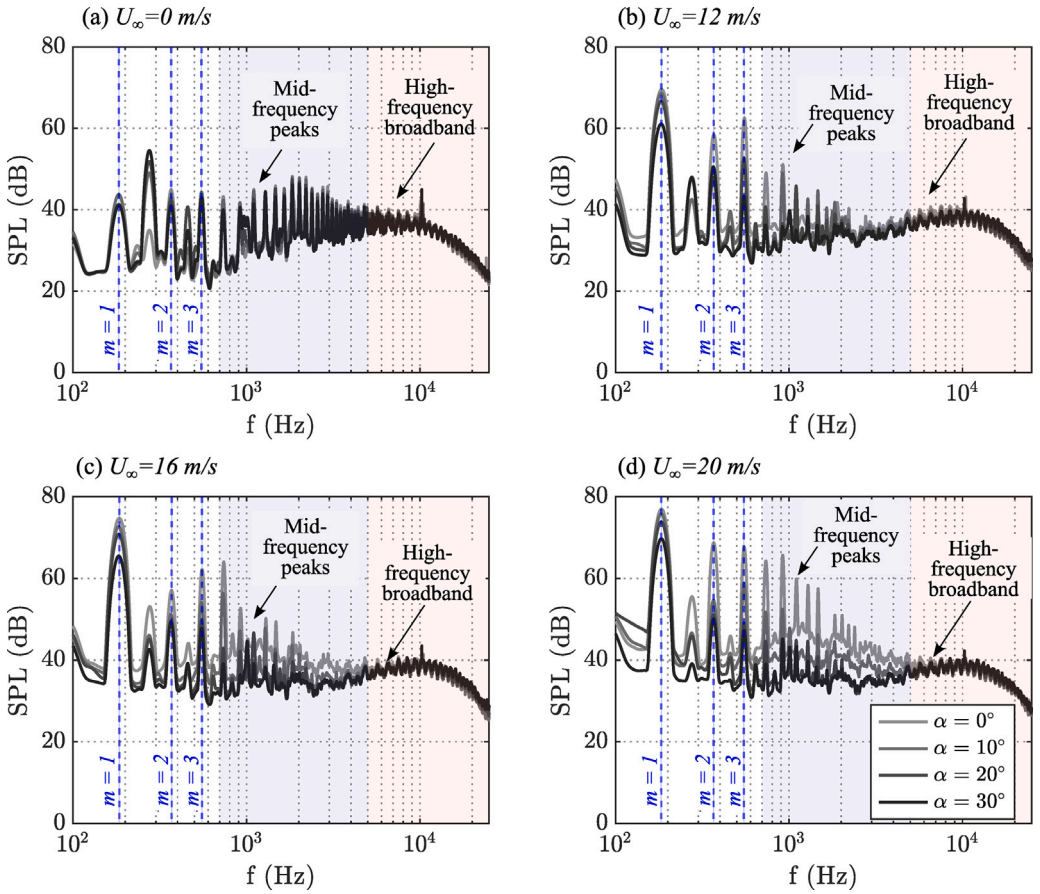


**Fig. 9.** Comparison of the far-field noise spectra at $\phi = 0°$ on the side array for (a) $U_\infty = 0$ m/s, (b) $U_\infty = 12$ m/s, (c) $U_\infty = 16$ m/s, and (d) $U_\infty = 20$ m/s.

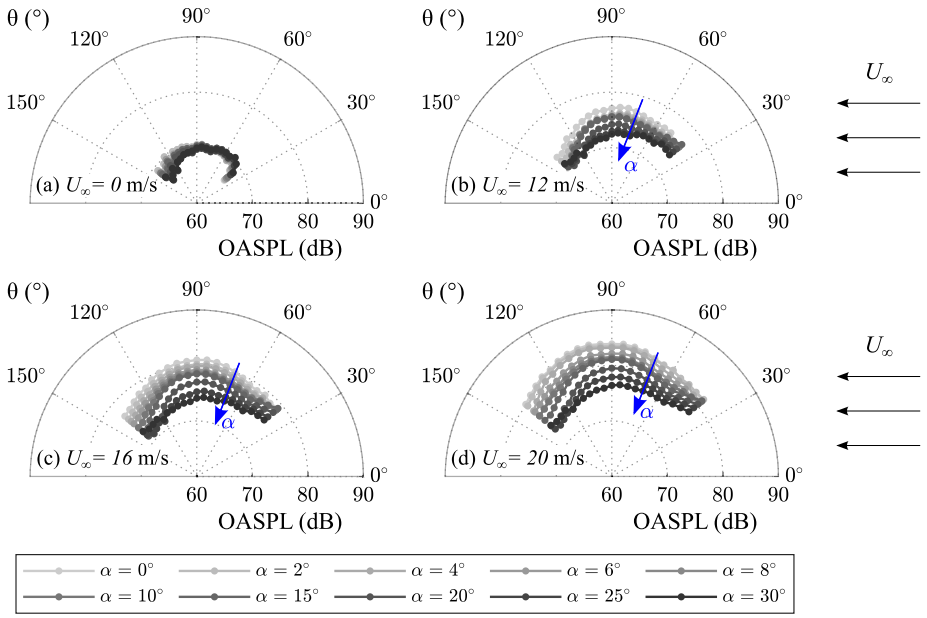


**Fig. 10.** OASPL directivity on top array for different tilting angles ranging between $0° \le \alpha \le 30°$ at an inflow velocity of (a) $U_\infty = 0$ m/s, (b) $U_\infty = 12$ m/s, (c) $U_\infty = 16$ m/s, and (d) $U_\infty = 20$ m/s.

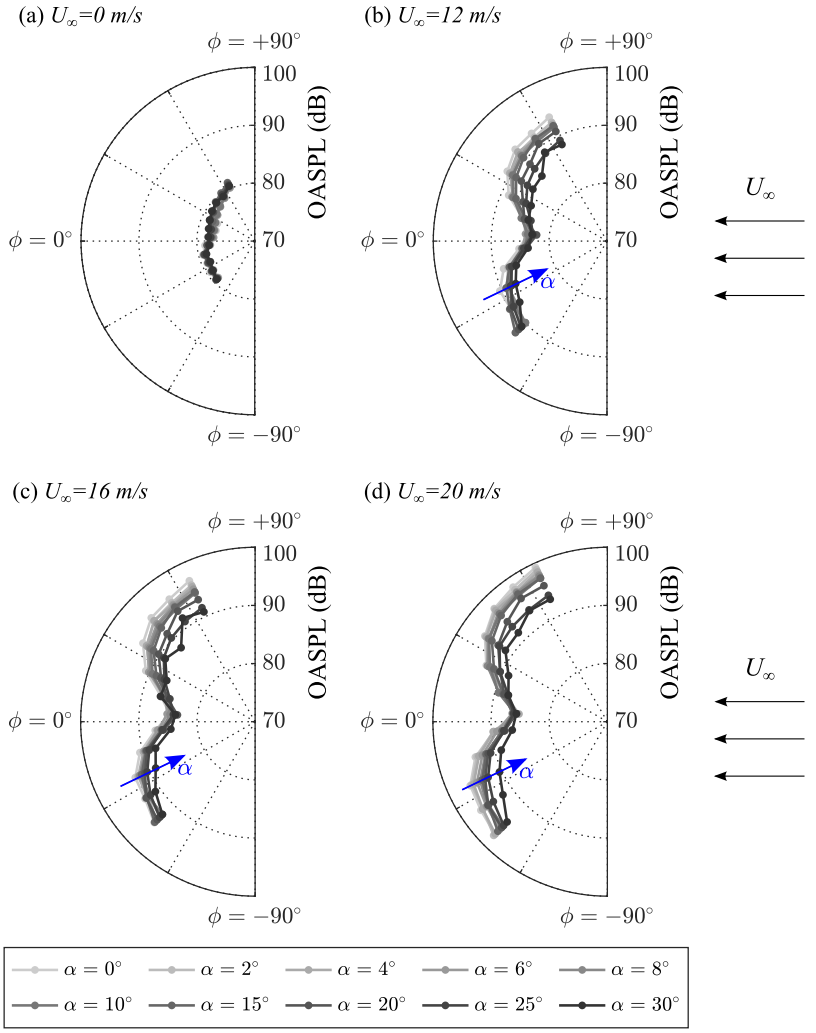


**Fig. 11.** OASPL directivity on side array for different tilting angles ranging between $0° \leq \alpha \leq 30°$ at an inflow velocity of (a) $U_\infty = 0$ m/s, (b) $U_\infty = 12$ m/s, (c) $U_\infty = 16$ m/s, and (d) $U_\infty = 20$ m/s.

Under non-zero inflow conditions, i.e. edge-wise inflow, a difference in the magnitude of OASPL with $\alpha$ is evident, which increases with the inflow velocity. Additionally, when observing the inflow velocity range of 12 to 20 m/s, the OASPL magnitude exhibits a decrease as the tilting angle increases. Specifically, from $\alpha = 0°$ to 30°, the reduction in OASPL of about 5 to 10 dB can be observed, indicating a significant noise reduction with the tilting angle. The directivity trends consistently indicate the maximum OASPL radiation near $\theta = 90°$ for each operation setting, and this is comparable across all presented rotor tilting angles.

Fig. 11 presents the OASPL directivity from the side observer positions between $\phi = +75°$ and $-55°$ for tilting positions ranging from $\alpha = 0°$ to 30°, at different inflow velocities of $U_\infty = 12$, 16, and 20 m/s. Under static thrust conditions, as shown in Fig. 11(a), there are no noticeable differences in OASPL can be observed across all side observation positions, consistent with the findings from the top array results in Fig. 10(a). As the inflow velocity increases, the radiation pattern changes, as shown in Fig. 11(b)–(d), where a dipolar directivity pattern emerges with the dipolar axis aligned near the rotor plane ($\phi = 0°$), i.e. the lowest noise radiation direction. The effect of tilting for the non-zero inflow cases is more significant outside the rotor plane ($\phi \neq 0°$), where the changes in OASPL can be clearly observed above the plane at $\phi = +45°$, with OASPL decreasing at higher tilting angle ($\alpha$), especially under higher inflow velocities. This trend of reduction in the OASPL with tilting angle is evident across all tested tilting positions between $\alpha = 0°$ to 30° at $U_\infty = 12$, 16, and 20 m/s inflow velocities, similar to what observed in Fig. 10.

Fig. 12 presents the trend of OASPL versus the thrust coefficient ($C_T$) under different operating conditions as a result of rotor tilting at the observation positions of $\theta = 90°$ and $\phi = 0°$. Each subplot represents the OASPL at six different rotor tilting angles, namely, $\alpha = 0°$, 10°, 15°, 20°, 25°, and 30°. These values are plotted against $C_T$ for a rotor operating at a constant rotational speed of $\Omega = 5500$ rpm and varying inflow velocities from $U_\infty = 8$ to 20 m/s. The blue-dashed lines in the figure demonstrate data trends at fixed inflow speed settings, aiding in the visual perception of trends across different rotor tilting angles.

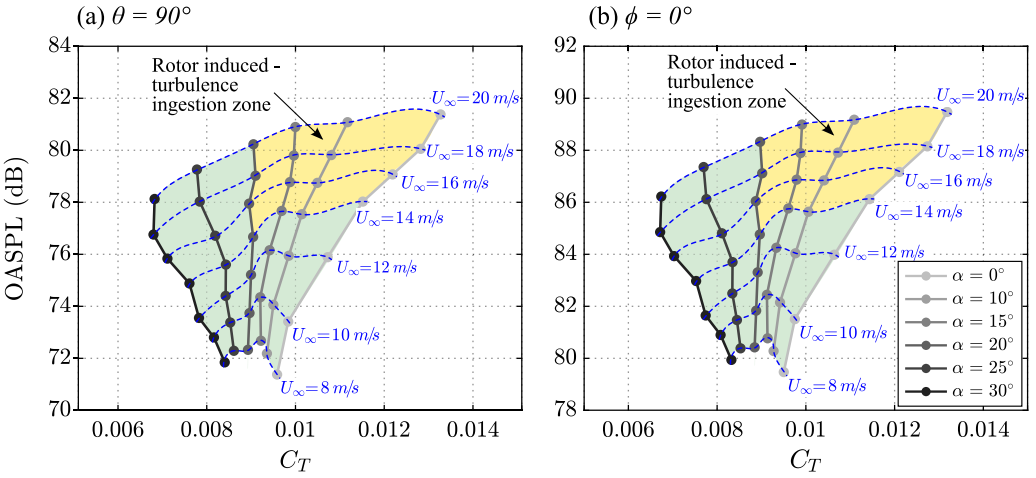


**Fig. 12.** Distribution of OASPL at the top and side array microphones of (a) $\theta = 90°$, and (b) $\phi = 0°$, respectively, plotted against the coefficient of thrust. The constant inflow speed settings for each case are highlighted as blue-dashed lines. (For interpretation of the references to colour in this figure legend, the reader is referred to the web version of this article.)

Based on the analyses of the noise data in Figs. 8 and 9, operational envelopes are constructed to highlight the influence of operational settings on the overall noise characteristics of the tilting rotor configuration. As can be seen, a region can be identified as the *"Rotor induced-turbulence ingestion zone"*, distinguished based on the increase in SPL values due to turbulence interaction observed Figs. 8 and 9. As can be seen in the spectra, there is a noticeable increase in broadband noise levels within the low to mid-frequency range, between 170 Hz to 7000 Hz. This increase is more pronounced at a lower tilt angle ($\alpha < 20°$) and high inflow speed, resulting in the ingestion of rotor self-induced turbulence. This observation is supported by our findings from Fig. 7, where significantly higher levels of $TKE$ were observed over the downstream half of the rotor for the cases with low tilt angle cases, leading to turbulence interaction with the rotor.

A distinctive pattern in the OASPL and $C_T$ distribution across various tilting angles emerged from the constructed operational envelopes, as presented in Fig. 12(a) and (b). Within the *"Rotor induced-turbulence ingestion zone"*, identified at $\alpha < 20°$, there is a direct correlation between increases in the OASPL and $C_T$. However, at $\alpha = 20°$, while the OASPL increases with inflow velocity, $C_T$ remains approximately constant at 0.009. Beyond $\alpha > 20°$, a reduction in OASPL is evident despite the increasing $C_T$. It is important to note that while results from other microphone locations are not presented here, OASPL distribution trends from other microphones across the arrays were analysed and found to exhibit similar and consistent patterns.

### 3.4. Blade passing frequency tonal noise

Figs. 13 and 14 present the noise directivity at the blade passing frequency ($m = 1$), as measured at the top plane and side plane arrays, respectively. Results are presented for a rotor operating under different inflow velocities of $U_\infty$ = 12, 16, and 20 m/s. Here, the sound pressure level $\text{SPL}_{m=1}$ is calculated by integrating the noise data over BPF–10 Hz and BPF+10 Hz frequency band.

In both Figs. 13 and 14, a consistent pattern is observed in the directivity trends of $\text{SPL}_{m=1}$ across all tested tilting angles. The far-field radiation in the top plane shows that regardless of the inflow velocity, the maximum radiation is consistently directed towards $\theta = 90°$ (See Fig. 13). Comparing the $\text{SPL}_{m=1}$ noise magnitudes in the top plane array, a difference of approximately 7 to 9 dB is observed between the $\alpha = 0°$ and $\alpha = 30°$ tilt angle cases. The results from side planes, on the other hand, show a slightly different distribution trend in the regions above and below the rotor's rotation planes, approximately at $\phi = +40°$ and $\phi = -40°$, respectively (See Fig. 14). As can be seen, the magnitude of $\text{SPL}_{m=1}$ as measured from the side plane indicates a reduction of up to 9 dB with increasing tilt angle from $\alpha = 0°$ to $\alpha = 30°$, particularly at the upper region above the plane of rotation. This observation is also consistent with the trend observed between the thrust coefficient and $\theta$ presented in Fig. 3, i.e. lower aerodynamic loading at higher tilting angle, which leads to reduced $m = 1$ noise.

The correlation between $\text{SPL}_{m=1}$ and $C_T$ is investigated to understand the relationship between the rotor's aerodynamic loading performance and the radiated tonal noise at the blade passing frequency. Figs. 15 and 16 present the SPL – $C_T$ plots for the microphone on the top and side plane arrays. The data correspond to an observation position at $\theta = 90°$ from the top array and two positions at $\phi = +40°$ and $\phi = -40°$ from the side array. At an inflow velocity of 20 m/s, the SPL – $C_T$ trend from the top plane array, shown in Fig. 15, indicates a change of approximately 7 dB in $SPL_{m=1}$ and around 0.0066 in $C_T$ (equivalent to 5 N in thrust) when the rotor transition from a vertical lift position of $\alpha = 0°$ to a forward tilt position of 30°.

For the side plane array at the same inflow velocity of 20 m/s above the rotation plane (i.e. $\phi = +40°$), as shown in Fig. 16(a), the tilting of the rotor leads to a change of around 5 dB in $SPL_{m=1}$ for the same thrust variation as observed in the top array. Conversely, below the rotation plane (i.e. $\phi = -40°$), the $SPL_{m=1}$ remain unchanged with only 1 dB of difference with varying

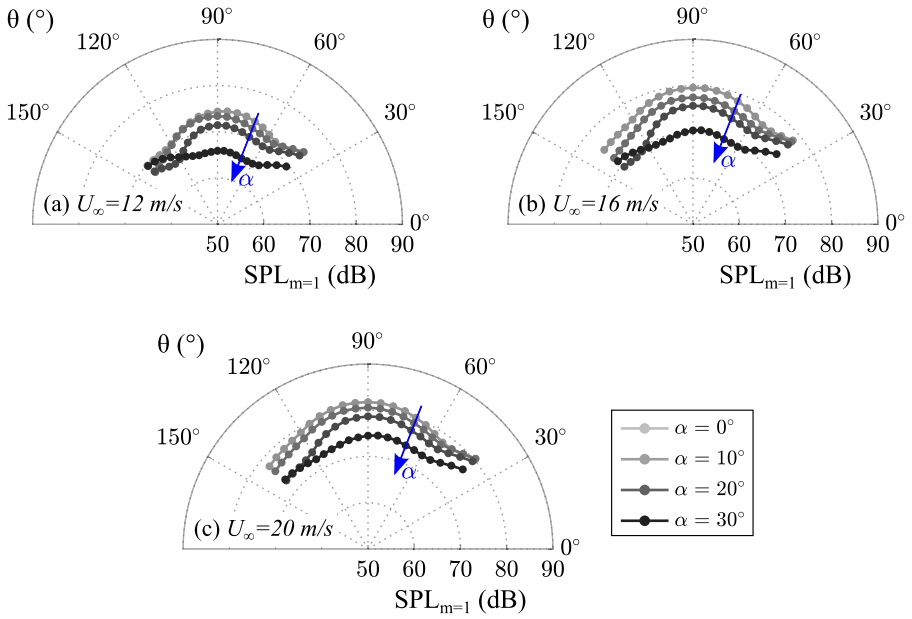


**Fig. 13.** The directivity of the sound pressure level at the blade passing frequency ($SPL_{m=1}$) as measured at the top plane arrays for the tilting rotor under (a) $U_\infty$ = 12 m/s, (b) $U_\infty$ = 16 m/s, and (c) $U_\infty$ = 20 m/s.

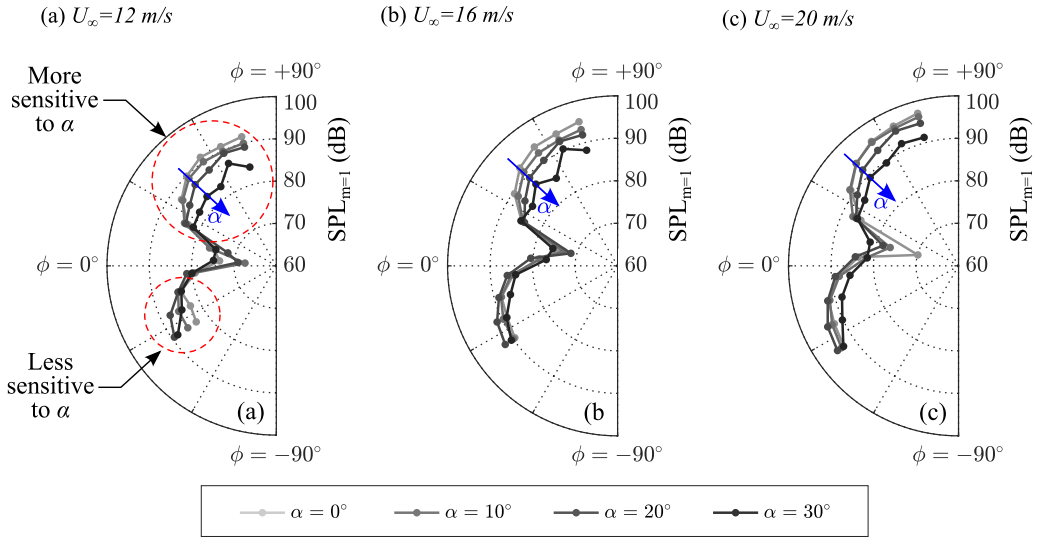


**Fig. 14.** The directivity of the sound pressure level at the blade passing frequency ($SPL_{m=1}$) as measured at the side plane array for the tilting rotor under (a) $U_\infty$ = 12 m/s, (b) $U_\infty$ = 16 m/s, and (c) $U_\infty$ = 20 m/s.

rotor tilt angle, as can be seen in Fig. 16(b). These observed trends SPL – $C_T$ show that rotor tilt influences BPF noise and thrust differently on the top and side planes. On the top plane, both noise and thrust change with rotor tilt, whereas on the side plane, specifically below the plane of rotation, the noise shows minimal change despite variations in tilt.

Following the narrowband SPL analysis at the fundamental blade passing frequency, the investigation is extended to include higher-order harmonics of the BPF. The frequencies of these harmonics are the integer multiples of the BPF, within the low-to-mid frequency range up to 7000 Hz. The sound pressure levels at these multiple harmonics of BPF (i.e. $SPL_{m=1}$ to $SPL_{m=6}$) were integrated within a narrow-band frequency window of ±10 Hz around the frequency of the harmonics.

Figs. 17 and 18 present the comparison of the SPL for the BPF (i.e. $m$ = 1) and the five harmonics (i.e. $m$ = 2 to 6) as functions of the rotor's thrust coefficient across different operating conditions. These SPL distributions, derived from the top (i.e. $\theta$ = 90°) and side plane (i.e. $\phi$ = +40°) observer positions, represent how SPL varies for each harmonic when the rotor operates at a constant rotational speed of 5500 rpm under varying tilting angles and inflow velocities ranging from 8 to 20 m/s. Given the complex

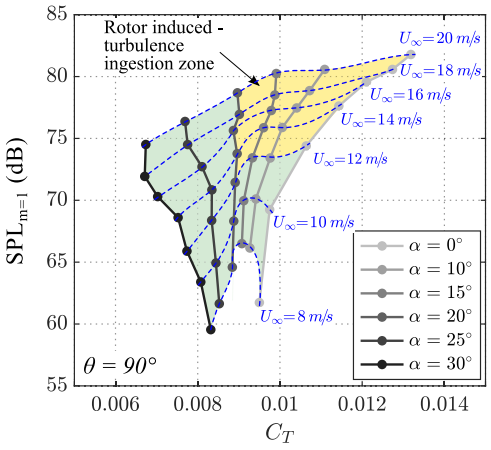


**Fig. 15.** Distribution of the sound pressure level of the blade passing frequency with respect to the thrust coefficient measured from the top array at $\theta = 90°$ microphone observation position.

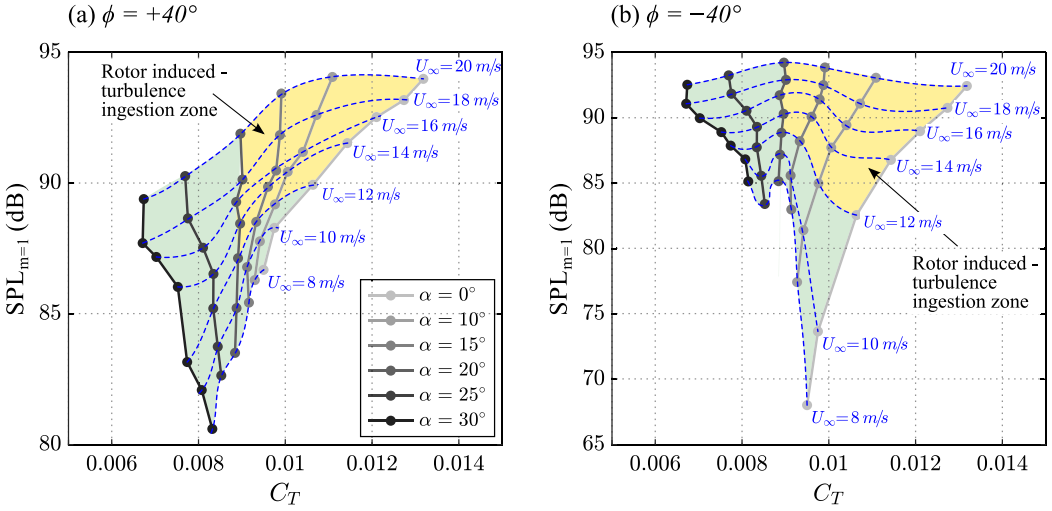


**Fig. 16.** Distribution of SPL calculated within BPF±10 Hz, presented at the side array microphones of (a) $\phi = +40°$, and (b) $\phi = -40°$, respectively, plotted against the thrust coefficient.

behaviour of the results with increasing inflow velocity, particularly for the higher harmonics response ($m > 1$), the results for each tilt angle are represented as scattered data points. However, to provide a sense of the overall trend, data points for the two extreme tilting angles, $\alpha = 0°$ and $\alpha = 30°$, are connected.

Based on Figs. 17 and 18, it is apparent that the magnitude of SPL, measured from the top and side planes of the rotor, is consistently higher across all harmonics when the rotor is upright ($\alpha = 0°$) than when tilted ($\alpha = 30°$). When assessing the difference in sound pressure level ($\Delta$SPL), a dependency on the rotor's tilt angle is evident. The magnitude of $\Delta$SPL clearly suggests that SPL is lower at the highest tilt position ($\alpha = 30°$) under increased inflow velocities than at $\alpha = 0°$. All examined harmonics of the blade passing frequency exhibit similar trends, where the associated SPL remains comparably lower for the case of larger tilt angle ($\alpha = 30°$) than at $\alpha = 0°$.

### 3.5. Time frequency analysis of noise signal

Until now, the analysis has utilised the Fourier Transform method to gain insights into the effects of rotor tilting on the spectral and directivity characteristics of the noise. However, this method is fundamentally frequency-oriented and inherently averages out the data, which effectively overlooks critical time-domain information. This section will now focus on the temporal characteristics of the radiated noise by employing wavelet analysis.

Fig. 19 presents the wavelet scalograms of the rotor noise obtained from the microphone at $\theta = 90°$ on the top array for varying tilt angle cases. The scalograms reflect a time-frequency distribution under constant operational settings of an inflow velocity of

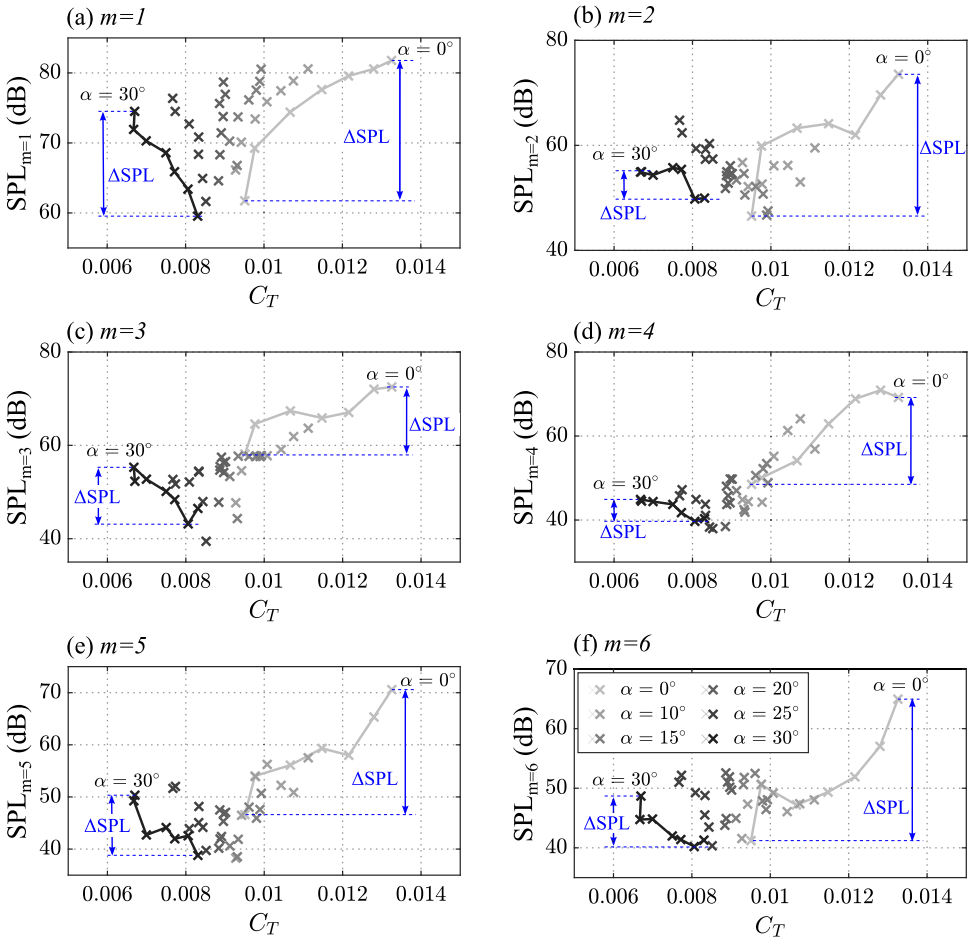


**Fig. 17.** Comparison of sound pressure levels across the fundamental BPF and five harmonics against the rotor's thrust coefficient, as measured from the top plane observation position of $\theta = 90°$: (a) $m = 1$, (b) $m = 2$, (c) $m = 3$, (d) $m = 4$, (e) $m = 5$ and (f) $m = 6$. To highlight the trend, solid lines connecting data for $\alpha = 0°$ and $\alpha = 30°$ are included. Data are obtained from a rotor operating at a constant rotational speed of 5500 rpm with varying tilting angles and inflow velocities ranging from 8 to 20 m/s.

16 m/s and a rotation speed of 5500 rpm. For brevity, only a limited time window is shown as the inherent trends of the signals are consistent throughout the entire time-series data. To ensure no physical phenomena with a long life span are missed in this analysis, the wavelet post-processing was performed using over 50 rotor revolutions. A comprehensive check has been conducted across the full sampling duration, confirming the uniformity of the trends. The vertical dotted lines indicate the rotor revolution time. Results are presented for a 0.04-s window, corresponding to approximately 3.6 rotor revolutions at a rotation speed of 5500 rpm.

As expected, a consistent characteristic of the signal is demonstrated at the fundamental blade passing frequency ($m = 1$) across all tilt angle cases, showing persistent behaviour at this frequency in contrast to the intermittent patterns observed at other ranges of frequencies. It is important to note that continuous lines in the scalograms are indicative of periodic signals [33]. However, the variation in wavelet scale intensity across different tilting angles reveals the impact of rotor tilting on the signal at BPF. The BPF signal response evolves gradually from a consistently high-intensity wavelet scale at $\alpha = 0°$ to a less intense state with increased tilt angle, as illustrated in Fig. 19 (a)–(d). This trend demonstrates the sensitivity of the signal's energy at BPF to the rotor's tilt angle. The energy levels at the fundamental BPF exhibit predominance behaviour that could potentially have implications on the perception of noise annoyance [34]. The effect of rotor tilting is also visible in the lower range of frequency, specifically at $f < 1000$ Hz, characterised by slightly less intense patterns than those at BPF. These intermittent signals are dominant at $\alpha = 0°$, spreading across multiple harmonics of BPF. However, the trend becomes less pronounced and eventually fades with increasing tilting angles. In the high-frequency range, approximately 5000 Hz $\leq f \leq$ 25,000 Hz, the results reveal evident intermittent signals. This intermittent behaviour, characterised by discontinuous amplitude modulation zones within the wavelet scales, is particularly apparent in the higher frequency ranges, which can significantly contribute to the perception of noise annoyance [35]. These high-frequency intermittent energy zones are clearly defined at $\alpha = 0°$, appearing twice in a rotation. However, as tilting angles increase, these zones become less noticeable, demonstrating a more random pattern, which suggests a change in the nature of high-frequency intermittency.

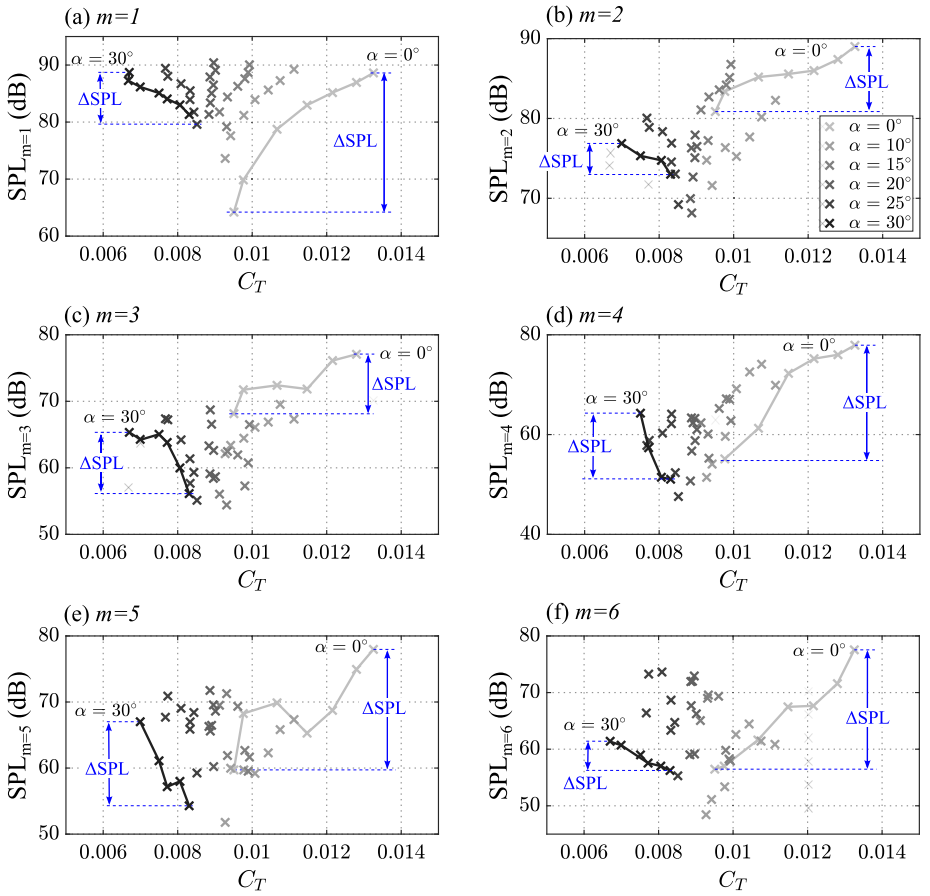


**Fig. 18.** Comparison of sound pressure levels across the fundamental BPF and five harmonics against the rotor's thrust coefficient, as measured from the side plane observation position of $\phi = +40°$: (a) $m = 1$, (b) $m = 2$, (c) $m = 3$, (d) $m = 4$, (e) $m = 5$ and (f) $m = 6$. To highlight the trend, solid lines connecting data for $\alpha = 0°$ and $\alpha = 30°$ are included. Data are obtained from a rotor operating at a constant rotational speed of 5500 rpm with varying tilting angles and inflow velocities ranging from 8 to 20 m/s.

Fig. 20 presents the wavelet scalograms for the rotor noise, measured from the side array microphones of $\phi = -40°$ under the same operational settings as the top array results. For brevity, only a limited time window is shown as the inherent trends of the signals are consistent throughout the entire time-series data. The time span for one complete revolution of the rotor blade is indicated within the boundary of the dotted black lines in the graph for clarity. Compared to the top array, the side array results also display a dominant and consistent signal for the fundamental blade passing frequency ($m = 1$) across all tilt angle cases. The impact of rotor tilting is apparent in the intensity of wavelet scales across different tilting angles. Specifically, the signal response at BPF is noticeably intense for $\alpha = 0°$ but gradually decreases as the tilt angle increases.

The side array results also revealed intermittent signals in the lower frequency range ($f < 1000$ Hz). These trends, which were prevalent over multiple harmonics, were dominant at $\alpha = 0°$ and diminished progressively as the tilt angle increased. This observation aligned with the top array data, reinforcing that the rotor's lower-frequency noise was susceptible to the tilt angle. Intermittent signals were also found to dominate at the high-frequency range at approximately 5,00 Hz $\leq f \leq$ 25,000 Hz, forming discontinuous zones of amplitude modulation. Contrary to the top array observations, where the zones became less noticeable with increasing tilting angles, on the side plane, they remained consistent regardless of the tilting angles. This persistence in behaviour highlights a notable difference in the intermittent nature of high-frequency signals based on the observation positions, which is important, given that these signals are significant factors in evaluating annoyance [35]. These findings emphasised the importance of considering observational positions when assessing potential noise impacts and their implications on noise perception.

## 4. Conclusion

In this comprehensive study, the impact of tilt angle on the noise characteristics of an isolated tilt-rotor system was analysed in various edgewise inflow conditions. The study showed that tilting of the rotor significantly impacts its thrust performance, where a consistent decrease in thrust was observed at increased tilt angle across all tested inflow velocities. The PIV flow measurements

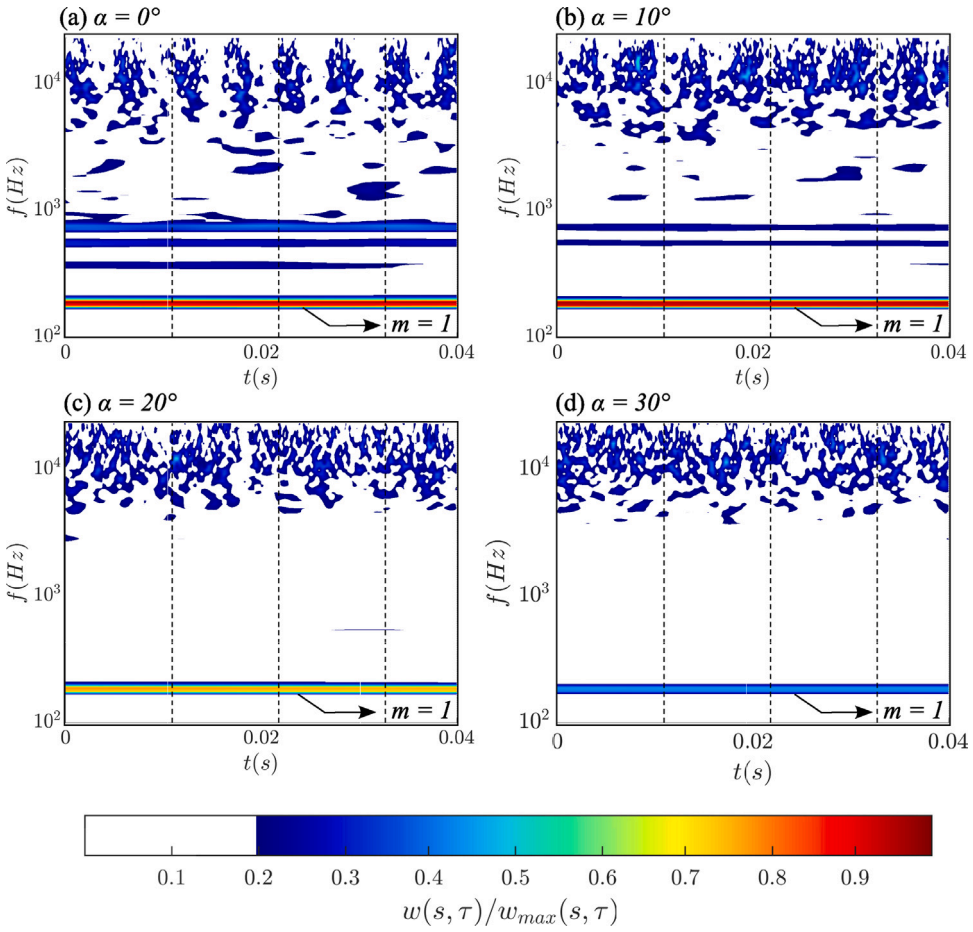


**Fig. 19.** The wavelet scalograms of the rotor noise, as measured at the top plane observer position of $\theta = 90°$, for tilting cases of (a) $\alpha = 0°$, (b) $\alpha = 10°$, and (c) $\alpha = 20°$, and (d) $\alpha = 30°$ under a constant operation inflow and rotation speed of 5500 rpm and 16 m/s.

revealed that the distribution of total velocity and mean turbulent kinetic energy within the field of view are both affected by the rotor tilt angle. At a lower tilting angle, there was an observable increase in turbulence energy in the flow, which gets re-ingested into the rotor. This, in turn, resulted in an increase in the noise radiation produced by the rotor. The spectral and time-dependent characteristics of the radiated noise exhibited a dependence on the rotor tilt angle, particularly at the blade passing frequency and its harmonics. The mid-frequency broadband noise levels were significantly higher for lower tilting angles compared to larger ones, especially at higher inflow speeds. However, the high-frequency noise remained relatively unaffected by the change in tilting angle. Furthermore, the direction of minimum radiation for the sound pressure level within a narrowband of the fundamental blade passing frequency ($SPL_{m=1}$) was consistently prevalent near the rotation plane, irrespective of the tilt angle, similar to the OASPL directivity trend.

The SPL – $C_T$ correlation analyses at the largest tested inflow velocity of 20 m/s revealed the influence of rotor tilting on the aerodynamic and aeroacoustic behaviours. As the rotor transitions from a vertical lift position of $\alpha = 0°$ to a forward tilt position of $\alpha = 30°$, an approximately 49% reduction in thrust was measured, and a 7 dB decrease in the sound pressure level at BPF ($SPL_{m=1}$) was observed in the top plane. This SPL – $C_T$ trend was similar to those observed from the side plane of rotation. In contrast, the $SPL_{m=1}$ radiated below the rotation plane remained nearly unaffected with rotor tilt changes. Further investigation into the time-frequency characteristics of the acoustic data revealed the temporal behaviour of the radiated noise across both lower and higher frequency ranges. In addition, persistent characteristics were evident at the BPF, while intermittent and transient characteristics were observed within the mid and higher frequency ranges, respectively.

## CRediT authorship contribution statement

**Nur Syafiqah Jamaluddin:** Conceptualization, Data curation, Formal analysis, Investigation, Methodology, Project administration, Resources, Software, Validation, Visualization, Writing – original draft, Writing – review & editing. **Alper Celik:** Data curation, Investigation, Methodology, Validation, Writing – original draft, Writing – review & editing. **Kabilan Baskaran:** Investigation,

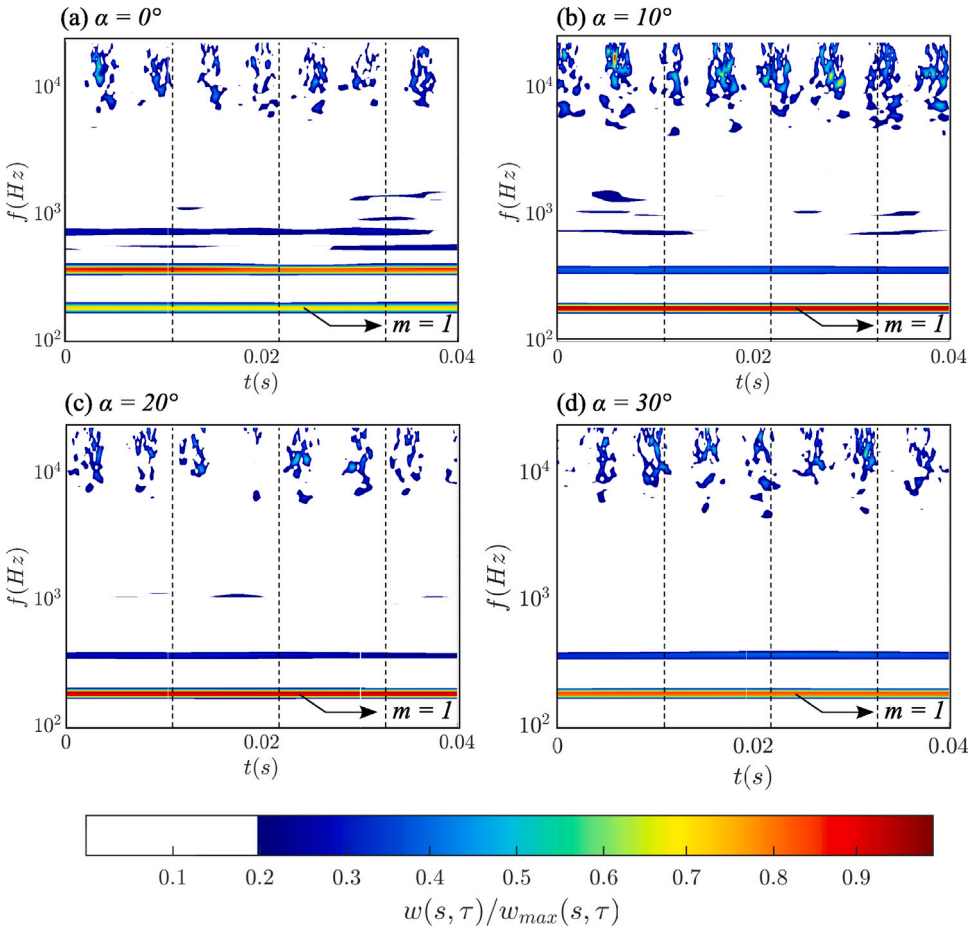


**Fig. 20.** The wavelet scalograms of the rotor noise, as measured at the side plane observer position of $\phi = +40°$, for tilting cases of (a) $\alpha = 0°$, (b) $\alpha = 10°$, and (c) $\alpha = 20°$, and (d) $\alpha = 30°$ under a constant operation inflow and rotation speed of 5500 rpm and 16 m/s.

Software, Writing – review & editing. **Djamel Rezgui:** Conceptualization, Writing – review & editing, Formal analysis, Funding acquisition, Project administration, Supervision, Writing – original draft. **Mahdi Azarpeyvand:** Formal analysis, Funding acquisition, Project administration, Supervision, Validation, Visualization, Writing – original draft, Writing – review & editing.

## Declaration of competing interest

The authors declare that they have no known competing financial interests or personal relationships that could have appeared to influence the work reported in this paper.

## Data availability

Data will be made available on request.

## Acknowledgements

The first author would like to acknowledge the financial support of Majlis Amanah Rakyat Malaysia. The second author would like to acknowledge the EPSRC (Engineering and Physical Sciences Research Council) for post-doctoral sponsorship at the University of Bristol from June 2020 to December 2021 (Grant No. EP/S013024/1). All authors would like to acknowledge Horizon 2020 research and innovation programme under grant agreement number 882842 (SilentProp project).

## References


[1] S. Kalakou, C. Marques, D. Prazeres, V. Agouridas, Citizens' attitudes towards technological innovations: The case of urban air mobility, Technol. Forecast. Soc. Change 187 (2023) 122200, http://dx.doi.org/10.1016/j.techfore.2022.122200.

[2] H. Eißfeldt, Sustainable urban air mobility supported with participatory noise sensing, Sustainability 12 (2020) 3320, http://dx.doi.org/10.3390/su12083320.

[3] S.A. Rizzi, D.L. Huff, D.D. Boyd, P. Bent, B.S. Henderson, K.A. Pascioni, D.C. Sargent, D.L. Josephson, M. Marsan, Urban Air Mobility Noise: Current Practice, Gaps, and Recommendations, Technical Report, NASA, 2020, NASA/TP-20205007433.

[4] F. Yunus, D. Casalino, F. Avallone, D. Ragni, Efficient prediction of urban air mobility noise in a vertiport environment, Aerosp. Sci. Technol. 139 (2023) 108410, http://dx.doi.org/10.1016/j.ast.2023.108410.

[5] L. Hanson, H.K. Jawahar, S.S. Vemuri, M. Azarpeyvand, Experimental investigation of propeller noise in ground effect, J. Sound Vib. 559 (2023) 117751, http://dx.doi.org/10.1016/j.jsv.2023.117751.

[6] G.J. Ducard, M. Allenspach, Review of designs and flight control techniques of hybrid and convertible VTOL UAVs, Aerosp. Sci. Technol. 118 (2021) 107035.

[7] L.A. Young, What is a tiltrotor? A fundamental reexamination of the tiltrotor aircraft design space, in: AHS International Technical Meeting on Aeromechanics Design for Transformative Vertical Flight, The Vertical Flight Society, 2018.

[8] A. Misra, S. Jayachandran, S. Kenche, A. Katoch, A. Suresh, E. Gundabattini, S.K. Selvaraj, A.A. Legesse, A review on vertical take-off and landing (VTOL) tilt-rotor and tilt wing unmanned aerial vehicles (UAVs), J. Eng. (2022) http://dx.doi.org/10.1155/2022/1803638.

[9] J.G. Leishman, Principles of Helicopter Aerodynamics, Cambridge University Press, 2000.

[10] J.C. Ho, H. Yeo, Assessment of comprehensive analysis predictions of helicopter rotor blade loads in forward flight, J. Fluids Struct. 68 (2017) 194–223, http://dx.doi.org/10.1016/j.jfluidstructs.2016.09.007.

[11] W.R. Splettstoesser, K.J. Schultz, R.M. Martin, Rotor blade-vortex interaction impulsive noise source localization, AIAA J. 28 (4) (1990) 593–600, http://dx.doi.org/10.2514/3.10434.

[12] N.S. Jamaluddin, A. Celik, K. Baskaran, D. Rezgui, M. Azarpeyvand, Experimental analysis of a propeller noise in turbulent flow, Phys. Fluids 35 (7) (2023) 075106, http://dx.doi.org/10.1063/5.0153326.

[13] S. Glegg, W. Devenport, Aeroacoustics of Low Mach Number Flows, Academic Press, 2017, pp. 399–436, http://dx.doi.org/10.1016/B978-0-12-809651-2.00016-3.

[14] M.B. Graf, E.M. Greitzer, F.E. Marble, O.P. Sharma, Effects of stator pressure field on upstream rotor performance, in: Turbo Expo: Power for Land, Sea, and Air, Vol. Volume 1: Aircraft Engine; Marine; Turbomachinery; Microturbines and Small Turbomachinery, 1999, http://dx.doi.org/10.1115/99-GT-099, V001T03A025.

[15] H.H. Hubbard, Aeroacoustics of Flight Vehicles: Theory and Practice. Volume 1. Noise Sources, Tech. Rep., National Aeronautics and Space Admin Langley Research Center, Hampton, Virginia, USA, 1991, NASA/TP-19920001380.

[16] E. Grande, G. Romani, D. Ragni, F. Avallone, D. Casalino, Aeroacoustic investigation of a propeller operating at low Reynolds numbers, AIAA J. 60 (2) (2022) 860–871, http://dx.doi.org/10.2514/1.J060611.

[17] W.A. Jordan, S. Narsipur, R. Deters, Aerodynamic and aeroacoustic performance of small UAV propellers in static conditions, in: AIAA Aviation 2020 Forum, in: AIAA Paper 2020-2595, 2020, http://dx.doi.org/10.2514/6.2020-2595.

[18] G. Sinibaldi, L. Marino, Experimental analysis on the noise of propellers for small UAV, Appl. Acoust. 74 (1) (2013) 79–88, http://dx.doi.org/10.1016/j.apacoust.2012.06.011.

[19] N.S. Zawodny, H. Haskin, Small propeller and rotor testing capabilities of the NASA Langley low speed aeroacoustic wind tunnel, in: Proceedings of the 23rd AIAA/CEAS Aeroacoustics Conference, in: AIAA Paper 2017-3709, 2016, http://dx.doi.org/10.2514/6.2017-3709.

[20] N.S. Zawodny, H. Haskin, D.M. Nark, Aerodynamic performance and acoustic measurements of a high-lift propeller in an isolated configuration, in: Proceedings of the 24th AIAA/CEAS Aeroacoustics Conference, in: AIAA Paper 2018-3448, 2018, http://dx.doi.org/10.2514/6.2018-3448.

[21] N.S. Zawodny, D.D. Boyd, Investigation of rotor–airframe interaction noise associated with small-scale rotary-wing unmanned aircraft systems, J. Am. Helicopter Soc. 65 (2019) 1–17, http://dx.doi.org/10.4050/JAHS.65.012007.

[22] C.E. Tinney, J. Valdez, Thrust and acoustic performance of small-scale, coaxial, corotating rotors in hover, AIAA J. 58 (4) (2020) 1657–1667, http://dx.doi.org/10.2514/1.J058489.

[23] Y. Yang, Y. Liu, Y. Li, E. Arcondoulis, Y. Wang, Aerodynamic and aeroacoustic performance of an isolated multicopter rotor during forward flight, AIAA J. 58 (3) (2020) 1171–1181, http://dx.doi.org/10.2514/1.J058459.

[24] Y. Mayer, H.K. Jawahar, M. Szoke, M. Azarpeyvand, Design of an aeroacoustic wind tunnel facility at the University of Bristol, in: 24th AIAA/CEAS Aeroacoustics Conference, in: AIAA Paper 2018-3138, 2018, http://dx.doi.org/10.2514/6.2018-3138.

[25] J. Johnston, R. Donham, W. Guinn, Propeller signatures and their use, J. Aircr. 18 (11) (1981) 934–942.

[26] B.H. Timmins, B.L. Smith, P.P. Vlachos, Automatic particle image velocimetry uncertainty quantification, in: ASME 2010 3rd Joint US-European Fluids Engineering Summer Meeting: Volume 1, Symposia – Parts A, B, and C, in: Fluids Engineering Division Summer Meeting, 2010, pp. 2811–2826, http://dx.doi.org/10.1115/FEDSM-ICNMM2010-30724, arXiv:https://asmedigitalcollection.asme.org/FEDSM/proceedings-pdf/FEDSM2010/49484/2811/4591563/2811_1.pdf.

[27] A. Sciacchitano, Uncertainty quantification in particle image velocimetry, Meas. Sci. Technol. 30 (9) (2019) 092001.

[28] W. Liu, J.A. Zagzebski, W. Liu, Trade-offs in data acquisition and processing parameters for backscatter and scatterer size estimations, IEEE Trans. Ultrason. Ferroelectr. Freq. Control 57 (2010) 340–352, http://dx.doi.org/10.1109/TUFFC.2010.1414.

[29] R. Camussi, S. Meloni, On the application of wavelet transform in jet aeroacoustics, Fluids 6 (8) (2021) http://dx.doi.org/10.3390/fluids6080299.

[30] G.L. Micci, R. Camussi, S. Meloni, C. Bogey, Intermittency and stochastic modeling of low- and High-Reynolds-Number compressible jets, AIAA J. 60 (3) (2022) 1983–1990, http://dx.doi.org/10.2514/1.J061128.

[31] N.S. Jamaluddin, A. Celik, K. Baskaran, D. Rezgui, M. Azarpeyvand, Experimental analysis of rotor blade noise in edgewise turbulence, Aerospace 10 (6) (2023) 502.

[32] J. Leishman, Principles of Helicopter Aerodynamics, in: Cambridge Aerospace Series, Cambridge University Press, 2016, URL: https://books.google.co.uk/books?id=uscAMQAACAAJ.

[33] S. Meloni, E. de Paola, E. Grande, D. Ragni, L.G. Stoica, A.D. Marco, R. Camussi, A wavelet-based separation method for tonal and broadband components of low Reynolds-number propeller noise, Meas. Sci. Technol. 34 (4) (2023) 044007, http://dx.doi.org/10.1088/1361-6501/acb071.

[34] U. Landström, E. Åkerlund, A. Kjellberg, M. Tesarz, Exposure levels, tonal components, and noise annoyance in working environments, Environ. Int. 21 (3) (1995) 265–275, http://dx.doi.org/10.1016/0160-4120(95)00017-F.

[35] D.Y. Gwak, D. Han, S. Lee, Sound quality factors influencing annoyance from hovering UAV, J. Sound Vib. 489 (2020) 115651, http://dx.doi.org/10.1016/j.jsv.2020.115651.